J. Mech. Phys. Solids 192 (2024) 105825

Contents lists available at ScienceDirect

Journal of the Mechanics and Physics of Solids

journal homepage: www.elsevier.com/locate/jmps

Hyperinelasticity. Part II: A stretch-based formulation

Afshin Anssari-Benam *

Cardiovascular Engineering Research Lab (CERL), School of Mechanical and Design Engineering, University of Portsmouth, Anglesea Road, Portsmouth, PO1 3DJ, United Kingdom

ARTICLE INFO

Keywords:
Large inelastic deformations
Hyperinelasticity
Comprehensive model
Principal stretches
Modelling non-deformation induced inelasticity

ABSTRACT

A generalisation of the *hyperinelasticity* modelling framework devised in Part I of this sequel is formulated here, by presenting a (principal) stretches-based hyperinelastic deformation energy function $W(\mathbf{F})$. This generalisation is based on the premise that the (principal) stretches λ_j may assume any arbitrary real-valued exponents, rather than being restricted to the prescriptive powers 2 and −2, as in principal invariants-based models. The motivation behind this extension is to reduce the overall number of model parameters and thereby increase the versatility of the application of the *hyperinelasticity* framework, as well as to provide a more universal model. The ensuing hyperinelastic model is then applied to a wide range of extant experimental datasets encompassing foams, glassy and semi-crystalline polymers, hydrogels and liquid crystal elastomers, over both elastic and inelastic deformation ranges including yield, softening and plateau, and hardening behaviours, under tensile and compressive deformations. Upon demonstrating the favourable simulation of the foregoing behaviours by the model, its application is then extended to account for other nuanced aspects of inelasticity such as the effects of rate of deformation, crystallinity volume and angle of printing in 3D printed lattice structures. This augmentation is done via devising a generalised modelling framework which allows for the incorporation of a generic tensorial (including rank zero scalar) field of inelasticity-inducing factors into the core model, resulting in the model parameters to evolve with an appropriate measure of the factor of interest; e.g., deformation rate, crystallinity volume ratio etc. The proposed modelling framework will be shown to capture these effects proficiently. Given the simplicity of this modelling approach, as essentially an extension in the application of hyperelasticity, its versatility of implementation, and the favourable capturing of both elastic and inelastic behaviours, the devised *hyperinelasticity* framework is presented for application to the large elastic and inelastic deformation of polymers and elastomers.

1. Introduction

In the prequel part (Anssari-Benam, 2024b), henceforth referred to as Part I, the *hyperinelasticity* framework for modelling elastic and inelastic behaviours of polymers using a single, unified, deformation energy $W(\mathbf{F})$ function was devised and presented. The said deformation energy function $W(\mathbf{F})$ represents an appropriate constitutive law to correlate the deformation energy with the deformation gradient $\mathbf{F}$, for the whole range of deformation including both elastic and inelastic ranges. As such, the constitutive parameters of this energy function $W(\mathbf{F})$ intrinsically determine and capture both the elastic and inelastic behaviours of the subject soft material.[1] This deformation energy $W(\mathbf{F})$ was termed the *core hyperinelastic* energy function: the term 'hyperinelastic' signifies

* Corresponding author.
E-mail address: afshin.anssari-benam@port.ac.uk.

[1] The inelastic behaviours of concern here are those that proceed the elastic behaviour in the primary loading path, with the progression of the deformation.

https://doi.org/10.1016/j.jmps.2024.105825
Received 12 July 2024; Received in revised form 10 August 2024; Accepted 11 August 2024
Available online 13 August 2024

large deformations of both elastic and inelastic attributions, and 'core' underlines the notion that W only incorporates the effect of deformation. The same terminology will be adopted here in this sequel too.

The primary elastic and inelastic behaviours that fall within the remit of the core hyperinelastic model $W(\mathbf{F})$, recounted from Part I, are: (a) the initial linear or nonlinear elastic behaviour, depending on the type of the polymer considered; (b) the nonlinear behaviour leading up to a peak, or an initial yielding, stress; (c) the drop in the stress often proceeded by a plateau, which signifies the occurrence of the yield; and (d) the hardening phase leading to the fracture/failure. The $W(\mathbf{F})$ function may then be augmented to incorporate additional effects such as the deformation rate by, e.g., assuming that the model parameters can evolve with; i.e., be a function of, the rate of deformation. Examples of the successful application of this approach were presented and analysed in Part I for a variety of datasets, polymers and deformations.

The considered *core hyperinelastic* energy function $W(\mathbf{F})$ in Part I was of the following binomial form:

$$W(\mathbf{F}) \equiv W(I_1, I_2) = \sum_{i=1} \frac{3(n_i-1)}{2n_i}\mu_i N_i \left[\frac{1}{3N_i(n_i-1)}(I_1-3)^{\beta_i} - \ln\left(\frac{I_1-3N_i}{3-3N_i}\right)^{\beta_i}\right] + \sum_{k=1} C_k \left[\left(\frac{I_2}{3}\right)^{\epsilon_k} - 1\right],$$

where I_1 and I_2 are the first and second principal invariants of the Cauchy – Green deformation tensor(s), $\mathbf{B}$ and/or $\mathbf{C}$, and $(I_3 = 1)$ due to the constraint of incompressibility. Here, μ_i and C_k are stress-like and N_i, n_i, β_i and ϵ_k are dimensionless model parameters. This model was first developed in Anssari-Benam (2024a), and its favourable application to the multiaxial deformation of a wide range of isotropic incompressible hyperelastic soft solids was demonstrated therein. The extension of the application of this model to *hyperinelasticity* too was successfully demonstrated in Part I, showing a favourable correlation with datasets from various polymers including semi-crystalline, glassy, foam, hydrogel and liquid crystal elastomer (LCE) etc samples.

However, some room for improvement may still be identified. First, as also pointed out in Part I, even the one-term expansion of this model embodies six parameters, which is within the remit identified by Ogden et al. (2004) for problems of nonlinear optimisation; namely that the obtained model parameter values (and thereby the best fit) from the process of fitting the model to the experimental data may not be unique. The practical implications of this non-uniqueness problem have also been noted by Zhan et al. (2023) in relation to microstructural models that include an excessive number of model parameters. It is therefore prudent to develop models that, while do not deter the fitting capability and quality, incorporate a reduced set of model parameters. Second, and somewhat related to the foregoing point, there is no mathematical reason for the exponents of the (principal) stretches λ_j to be prescriptively restricted to powers 2 and -2 (Treloar, 1976), as is the case with I_1 and I_2 by definition. Indeed, while the principal invariants I_j, $j = 1, 2, 3$, may have geometrical interpretations (Kearsley, 1989), the appearance of power of 2 in the exponent of λ_j is due to the assumption of affine deformation of the chains (see, e.g., Arruda and Boyce, 1993), and the appearance of the latter exponent stems from considerations of topological constraints (see, e.g., Fried (2002); Khiêm and Itskov (2016); Anssari-Benam et al., 2021). A more general approach, even from the perspective of connecting the macro-level behaviour to the micro-level deformation (see Puglisi and Saccomandi (2016) for an overview), may be to relax those prescriptive powers and allow for the (principal) stretches λ_j to assume any generic real valued exponents.

In view of the foregoing, in this sequel I set to propose a further generalisation of the model considered in Part I, and present a core hyperinelastic function $W(\mathbf{F})$ based on the principal stretches λ_j. In doing so, as will be discussed in the next section, not only I endeavour to address the aforementioned two points of improvement, but also another step will be made towards reaching a more universal deformation energy function $W(\mathbf{F})$, in both hyperelasticity and *hyperinelasticity* domains, which most (if not eventually all) other models in the literature are a subset, or a special form, of. This latter step alone will hopefully aid simplifying the literature to date, and reduce the confusion therein, as regards to the choice for a *suitable* strain energy function to model the finite deformation (both elastic and inelastic) of elastomers and polymers, since most those models can be replaced by the more generic, universal *parent* model that will be presented herein.

For consistency of presentation, and to provide a basis for comparison with the modelling results in Part I, the datasets considered here for the purpose of modelling the core *hyperinelastic* behaviour in the primary loading path are mostly those also used in that prequel. These include: (i) a high density polyethylene sample under uniaxial tensile deformation due to Ayoub et al. (2010) by way of exemplifying a semi-crystalline polymer; (ii) the poly(methyl methacrylate) specimens of Uchida et al. (2022) under tensile deformation as an example of glassy polymers; (iii) open- and closed-cell polyurethane and closed-cell polystyrene samples under uniaxial compression due to Lee et al. (2020) as representative examples of polymeric foams; (iv) the quadruple-network hydrogel specimens of Vernerey et al. (2018) under uniaxial tension to showcase the application of the proposed framework to the large deformation of multi-network hydrogels; and (v) isotropic-genesis polydomain LCE specimens under uniaxial deformation due to Tokumoto et al. (2021). To those examples is added here a new dataset on: (vi) high-impact polystyrene samples under uniaxial tension due to G'Sell et al. (2002), as a further example on the application of the model to glassy thermoplastic polymers.

Upon the successful application of the proposed model to the foregoing core hyperinelastic behaviours, the presented $W(\mathbf{F})$ function will be extended for incorporation of additional effects on elastic and inelastic behaviours of soft specimens. Three specific additional effects will be considered: (vii) the effect of deformation rate via the dataset of Lee et al. (2020) on open-cell polyurethane specimens and that of Pan et al. (2024) on amorphous polylactic acid (PLA) samples, as representatives of foams and glassy polymer behaviours; (viii) the effect of crystallinity volume ratio as given by Abdul-Hameed et al. (2014) and Yan et al. (2021) for semi-crystalline polymers; and (ix) the effect of printing angle on the mechanical behaviour of additively manufactured (3D printed) lattice structures made of curable photosensitive resin, due to Guo et al. (2024). A general framework for this extension of the $W(\mathbf{F})$

model to incorporate the foregoing additional inelastic effects will be devised and presented in this sequel, as a generalisation of the modelling approach of Anssari-Benam and Hossain (2023); i.e., to consider that the constitutive parameters in $W(\mathbf{F})$ evolve, or are a function of, the variable effect of interest, be it deformation rate, crystallinity volume ratio or the angle of 3D printing. Using the aforementioned datasets and approach, the favourable application of the *augmented* model to capturing the designated effects on the large elastic and inelastic behaviours of the subject polymers will be presented. This diverse range of additional factors, i.e., additional to the pure deformation gradient, provides a good variety for testing and showcasing the capability of the pursued modelling approach for extending the core hyperinelastic function $W(\mathbf{F})$ to incorporate those effects.

The formulation of the new (principal) stretches-based *core hyperinelastic* model will be presented in Section 2. The application of the model to elastic and inelastic behaviours of the various polymeric/elastomeric specimens outlined in (i) to (vi), in the primary loading path, will be considered in Section 3. The generalised framework for augmenting the *core* model to incorporate the effects of deformation rate, crystallinity ratio and the 3D printing angle will be detailed in Section 4, along with the application of the ensuing model(s) to the designated datasets in (vii) to (ix). The favourable modelling results in capturing the complex large inelastic behaviours of the considered wide range of polymers and elastomers, for both *core hyperinelastic* and extended modelling frameworks will be demonstrated in each respective section. Given the simplicity of the presented modelling framework, the versatility of its application, the degree of universality of the proposed model in terms of both being a *parent* to most other strain energy functions in the literature and its applicability to a wide range of various polymer types, and the favourability of the results, the devised *hyperinelastic* model is proposed by way of conclusion in Section 5 for a flexible application to the large elastic and inelastic behaviours of polymers and elastomers.

2. The (principal) stretched-based *core hyperinelastic* model

The motivation behind seeking a (principal) stretches-based model as the *core hyperinelastic* function is to remove the overtly prescriptive assumption that the value of the exponents of the principal stretches λ_j must necessarily be restricted to 2 and/or -2. This undertaking, as will be shown in the proceeding, possesses two advantages. First, and the more obvious, advantage is that the ensuing $W(\mathbf{F})$ function will be of a more generalised functional form, whereby the dependency on the principal invariants I_1 and I_2, such as in the model of Part I, may be recovered as a particular subset when the exponents α_i $(i=1,2)$ of the principal stretches λ_j $(j=1,2,3)$ are $\alpha_i=2$ and -2, respectively. Second, and perhaps the more practical, advantage is the possibility to reduce the binomial form of $W(I_1,I_2)$ to a monomial form $W\left(\lambda_j^{\alpha_i}\right)$, and thereby reduce the number of model parameters involved. The latter advantage point will help decrease, though not completely alleviate, the non-uniqueness issue identified by Ogden et al. (2004) in nonlinear fittings, while the former point provides a significant step towards achieving a more *universal* hyperinelastic[2] deformation energy function.

2.1. Model formalism

It may be instructive to start by recalling the notion put forward in Anssari-Benam (2021) that, it is possible to derive a new class of non-Gaussian constitutive models by constructing their response function(s) using *higher order* Padé approximants. To that end, the response function $2W_1$ of the model in Part I, where the subscript 1 denotes the partial derivative of W with respect to I_1, is of the general order $[\beta_i/1]$ in I_1 (Anssari-Benam, 2024a). See also Horgan and Saccomandi (2003) for the justification of the logarithmic term when using higher order rational approximations. This higher order rational approximant, then, naturally results in the model being a *parent* to many of the existing models in literature. That is, many of the models in the literature are only a subset, and less accurate, manifestation of this more *universal* model.

In this spirit, an even more generalisation, and a higher order approximant in λ_j, may be arrived at by considering the general invariants λ_j^{α} rather than the principal invariants I_1 and/or I_2, and arrive at the following principal stretches-based model in this sequel:

$$W(\mathbf{F})=\sum_{i=1}\frac{3\left(n_i-1\right)}{2n_i}\mu_i N_i\left[\frac{1}{3N_i\left(n_i-1\right)}\left(\lambda_1^{\alpha_i}+\lambda_2^{\alpha_i}+\lambda_3^{\alpha_i}-3\right)^{\beta_i}-\ln\left(\frac{\lambda_1^{\alpha_i}+\lambda_2^{\alpha_i}+\lambda_3^{\alpha_i}-3N_i}{3-3N_i}\right)^{\beta_i}\right], \tag{1}$$

where $\lambda_1\lambda_2\lambda_3=1$ to enforce the condition of incompressibility. Here, μ_i is a stress-like, and N_i, n_i, α_i and β_i are dimensionless, model parameters subjected to n_i, $N_i\in\mathbb{R}^+$, and α_i, $\beta_i\in\mathbb{R}$. The infinitesimal shear modulus μ_0 is: $\mu_0=\sum_{i=1}\frac{\mu_i\alpha_i^2\beta_i N_i\left(1-n_i\right)}{4n_i\left(1-N_i\right)}$.

While the proposed model in Eq. (1) may be expanded to any number of terms desired, it is expedient from the view point of versatility and finding a unique optimum fit to keep the number of terms to a minimum. As we shall see in Sections 3 and 4, for many applications of inelasticity, a two-term expansion of the model will suffice to capture the whole elastic and inelastic deformations.

[2] Or, for that matter, a *universal* hyperelastic strain energy function too.

2.2. Comprehensibility of the model

The $W(\mathbf{F})$ deformation energy function in Eq. (1), while maintaining a simple functional form, is a proficient generalisation of many of the existing strain energies in the literature. A two-term expansion of $W(\mathbf{F})$ with $\alpha_1 = 2$ and $\alpha_2 = -2$, at the limit $n_2 \to \infty$ results in:

$$\lim_{n_2\to\infty} W(\mathbf{F}) = \frac{3\left(n_1-1\right)}{2n_1}\,\mu_1 N_1\left[\frac{1}{3N_1\left(n_1-1\right)}\left(\lambda_1^2+\lambda_2^2+\lambda_3^2-3\right)^{\beta_1} - \ln\left(\frac{\lambda_1^2+\lambda_2^2+\lambda_3^2-3N_1}{3-3N_1}\right)^{\beta_1}\right] + \frac{\mu_2}{2}\left(\lambda_1^{-2}+\lambda_2^{-2}+\lambda_3^{-2}-3\right)^{\beta_2}, \tag{2}$$

which, in view of I_1 and I_2 principal invariants, can be immediately re-written as:

$$\lim_{n_2\to\infty} W(\mathbf{F}) = \frac{3\left(n_1-1\right)}{2n_1}\,\mu_1 N_1\left[\frac{1}{3N_1\left(n_1-1\right)}\left(I_1-3\right)^{\beta_1} - \ln\left(\frac{I_1-3N_1}{3-3N_1}\right)^{\beta_1}\right] + \frac{\mu_2}{2}\left(I_2-3\right)^{\beta_2}. \tag{3}$$

This function is homologous[3] to the hyperinelastic model in Part I; i.e., the $W(\mathbf{F})$ function in Eq. (1) is *parent* to the deformation energy W akin to that of Part I, in Eq. (3).

The non-separable principal stretches-based model W_{AB} of Anssari-Benam (2023) is straightforwardly obtained from the $W(\mathbf{F})$ function in Eq. (1) by setting $\beta_i = 1$:

$$W(\mathbf{F}) \overset{\beta_i=1}{\equiv\equiv} W_{AB} = \sum_{i=1}^{} \frac{3\left(n_i-1\right)}{2n_i}\,\mu_i N_i\left[\frac{1}{3N_i\left(n_i-1\right)}\left(\lambda_1^{\alpha_i}+\lambda_2^{\alpha_i}+\lambda_3^{\alpha_i}-3\right) - \ln\left(\frac{\lambda_1^{\alpha_i}+\lambda_2^{\alpha_i}+\lambda_3^{\alpha_i}-3N_i}{3-3N_i}\right)\right], \tag{4}$$

and by virtue of this fact, the $W(\mathbf{F})$ function is therefore *parent* to all models that W_{AB} is; namely from the classical neo-Hookean model (Treloar, 1943) to that of Mooney–Rivlin (Rivlin, 1948), the Ogden model (Ogden, 1972) and the limiting chain extensibility model of Gent (Gent, 1996), *inter alia*. The demonstration of how the foregoing models are all recovered from W_{AB}, itself a special case of the proposed $W(\mathbf{F})$ model in Eq. (1), has been presented in Anssari-Benam (2023). By way of example, I note that the one-term expansion of $W(\mathbf{F})$ at the limit $n \to \infty$ with $\beta = 1$ results in:

$$\lim_{n\to\infty} W(\mathbf{F}) = -6\,\frac{N-1}{\alpha^2}\,\mu_0 \ln\left(-\frac{\lambda_1^{\alpha}+\lambda_2^{\alpha}+\lambda_3^{\alpha}-3N}{3N-3}\right). \tag{5}$$

By using the change of variable $J_m = 3N - 3$, Eq. (5) is re-written as:

$$\lim_{n\to\infty} W(\mathbf{F}) = -2\,\frac{J_m}{\alpha^2}\,\mu_0 \ln\left(1-\frac{\lambda_1^{\alpha}+\lambda_2^{\alpha}+\lambda_3^{\alpha}-3}{J_m}\right), \tag{6}$$

which, on setting $\alpha = 2$ readily recovers the Gent model. Similarly, at the limit $N_i \to \infty$, the $W(\mathbf{F})$ model of Eq. (1) reduces to:

$$\lim_{N_i\to\infty} W(\mathbf{F}) = \sum_{i=1}^{} \frac{\mu_i}{2}\left(\lambda_1^{\alpha_i}+\lambda_2^{\alpha_i}+\lambda_3^{\alpha_i}-3\right), \tag{7}$$

which clearly is an alternative manifestation of the Ogden model with the change of variable as: $\mu_i = \dfrac{2\mu_i^{og}}{\alpha_i}$. I should also note the class of second-invariant materials (SIMs), i.e., constitutive models where the strain–energy function is exclusively a function of I_2, recently devised by Kuhl and Goriely (2024), are also straightforwardly recovered as special subsets from the $W(\mathbf{F})$ model in Eq. (1), on setting $\alpha_i = -2$ at various limits of n and/or N, similar to their first-invariant counterparts.

These attributes indicate the *universality* of the proposed $W(\mathbf{F})$ function in Eq. (1), in that most of the existing deformation energy functions are a subset; i.e., an approximation, of the this *parent* model. As such, all the specific behaviours that are addressed by any of those individual models; e.g., hardening and/or softening effects etc, are contained within the proposed $W(\mathbf{F})$ model, and with higher accuracy. Moreover, the unit expansion term of $W(\mathbf{F})$ contains a lower number of model parameters compared with the model in Part I. These advantages should render the model in Eq. (1) a more comprehensive and flexible choice for application to the large deformation of polymers and elastomers.

3. Correlation with experimental data

The *core hyperinelastic* $W(\mathbf{F})$ function in Eq. (1) will now be applied to extant experimental datasets of various polymer/elastomer types, including semi-crystalline and glassy polymers, foams, hydrogels and isotropic-genesis polydomain LCEs. To provide a comparative basis for the reader, the datasets considered here are those of Part I, with an additional dataset on glassy thermoplastic polymers to showcase the broader applicability of the proposed model beyond what was presented in Part I.

[3] Note that the I_2 term in the W function in Part I is of the form $I_2 = \mu_2\left[\left(\frac{I_2}{3}\right)^{\beta_2} - 1\right]$.

The behaviours of concern, to be addressed by the $W(\mathbf{F})$ model of Eq. (1) in this section, pertain to the isothermal elastic and inelastic behaviours of the subject specimens, in the primary loading path. The body of the literature, including the experimental studies that are considered here in this work, employ uniaxial deformation (either tensile or compressive) to characterise those elastic and inelastic behaviours. To this end, we shall derive the $T_{uni} - \lambda$ relationship under uniaxial deformation from the $W(\mathbf{F})$ model in Eq. (1). Accordingly, on using the representation formula (Ogden, 1997):

$$T_j = \lambda_j \frac{\partial W}{\partial \lambda_j} - p, \tag{8}$$

where p is the arbitrary hydrostatic pressure enforcing the condition of incompressibility, and subject to the assumption of plane stress $(T_{33} = 0)$, we find:

$$T_{uni} = \sum_{i=1} \frac{\mu_i \alpha_i \beta_i}{2n_i} \frac{\left(\lambda^{\alpha_i} + 2\lambda^{-0.5\alpha_i} - 3\right)^{\beta_i 1} \left(\lambda^{\alpha_i} + 2\lambda^{-0.5\alpha_i}\ 3N_i\right) 3N_i \left(n_i - 1\right)}{\lambda^{\alpha_i} + 2\lambda^{-0.5\alpha_i}\ 3N_i} \left(\lambda^{\alpha_i} - \frac{1}{\lambda^{0.5\alpha_i}}\right), \tag{9}$$

Note that in uniaxial deformation, $\lambda_1 = \lambda$, $\lambda_2 = \lambda_3 = \lambda^{-0.5}$.

Depending on the desired number of terms,[4] the relationship in Eq. (9) is fitted to each experimental dataset. The optimal fit is obtained by minimising the residual sum of squares (RSS) function defined as: $\text{RSS} = \sum_x \left(T^{model} - T^{experiment}\right)_x^2$, where x is the number of datapoints and T is the Cauchy stress. The minimisation is performed via an in-house developed code in MATLAB®, using the genetic algorithm (GA) function. The datapoint in the undeformed state, i.e., $(\lambda = 1, T = 0)$, was removed from each dataset before the fitting process in order to eliminate the numerical instabilities that may arise in cases when $\beta < 1$; i.e., to avoid division by zero at point $\lambda = 1$. The coefficient of determination R^2 values, along with the relative error plots, are also presented as a measure of the goodness of the obtained fits.

3.1. Semi-crystalline polymers

As a representative example of the application of the model to semi-crystalline polymers, here we consider the same dataset of Ayoub et al. (2010) as in Part I, on a high density polyethylene sample under uniaxial tensile deformation. 'Hourglass-shaped' specimens were prepared for the tests, to enable detecting the initiation of necking in the mid-plane of the samples. The tests were performed via an Instron© electromechanical testing machine, coupled with a videometric testing system (videotraction©) consisting of a CCD camera to record the current value of the smallest sample cross-section where necking is initiated. A representative illustration of that setup is presented in Fig. 1.

The two-term expansion of the model $W(\mathbf{F})$ was empirically observed to provide favourable fits to this dataset; i.e., the two-term expansion $(i = 1, 2)$ of the relationship in Eq. (9) was used to fit with this dataset. The modelling results, with the ensuing relative error plot, are presented in Fig. 2. Table 1 summarises the obtained model parameter values. Comparing these results with that in Part I using the two-term expansion of the model therein, it is immediately observed that the $W(\mathbf{F})$ model in Eq. (1) here provides an improved fit to the data, with lower number of model parameters (10 parameters here versus 12 for the model in Part I) and a higher R^2 value. The tabulated numerical datapoints of this dataset have been provided in Part I.

3.2. Glassy polymers

Ames et al. (2009) present experimental data on the large deformation of poly(methyl methacrylate) specimens under uniaxial tension. Here, I consider their results, reproduced by Uchida et al. (2022), as an exemplar dataset for application of the proposed $W(\mathbf{F})$ model to the elastic and inelastic behaviours of glassy polymers. Dumbbell-shaped specimens formed using silicone moulds were prepared and utilised for monotonic tensile tests via a compact tensile and compression tester (IMC-18E0, Imoto Machinery Co., Ltd.). See the inset in Fig. 3a for a schematic representation and the geometry of the specimens. The one-term expansion of the model; i.e., $i = 1$ in Eq. (9), was used for fitting with the data. The plots in Fig. 3 illustrate the modelling results, and Table 2 contains the identified model parameter values. The suitability of the model for capturing the finite deformation of this specimen, in both elastic and inelastic deformation ranges, is evident from the results, with an R^2 value in excess of 0.99. Compared with the results in Part I, the model here provides the same favourable quality of fit, but with one less model parameter (5 versus the 6 parameters of the model in Part I). The numerical values for this dataset have been given in Part I.

As a further example of the application of the model to glassy thermoplastic polymers, next I present the modelling results for the high-impact polystyrene samples of G'Sell et al. (2002) under uniaxial deformation. Parallelepiped specimens of dimensions $63 \times 12 \times 4$ mm^3 were prepared, and tested via a VideoTraction© system (Apollor, Vandoeuvre, France), which is capable of detecting diffuse necking during a tensile test. The inset in Fig. 4a shows an illustration of the sample in deformation. This dataset was not considered in Part I, and the numerical values of the datapoints have been tabulated and provided in Table A.1 of Appendix. A two-term expansion of the model in Eq. (9) was deemed sufficient for capturing this dataset, producing a R^2 value of 0.99. The plots in Fig. 4 present the modelling results. The model parameter values are provided in Table 3.

[4] Note that the number of terms $(i = 1, 2, 3, \ldots)$ used for fitting with a given dataset is a judicious empirical choice, determined via a balance on behalf of the modeller between the goodness of the fit and the number of model parameters.

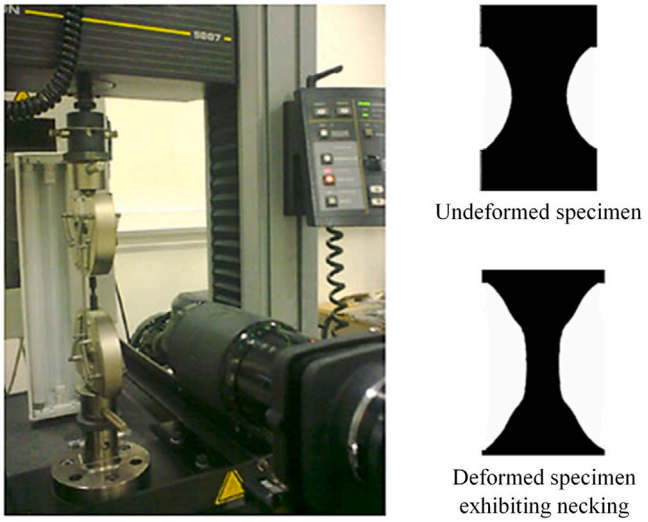

Fig. 1. The experimental system, and the schematic representation of the samples, used in the study of Ayoub et al. (2010); adapted with permission.

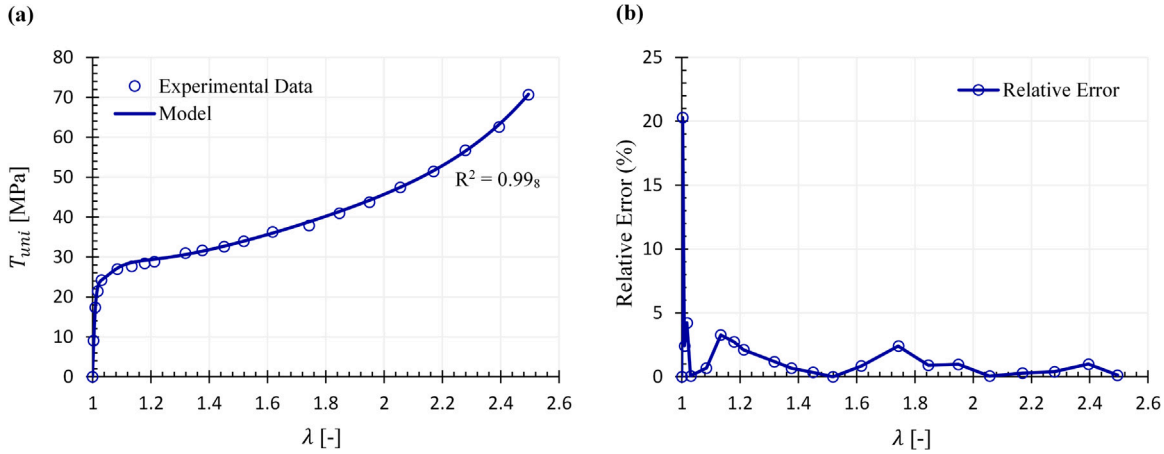

Fig. 2. Modelling results for the semi-crystalline polymer samples of Ayoub et al. (2010): (a) the fitting of the two-term expansion of the model with the data; and (b) the ensuing relative errors.

Table 1
The obtained model parameter values for the elastic and inelastic deformations of high density polyethylene samples due to Ayoub et al. (2010).

μ_1 [MPa]	N_1 [–]	n_1 [–]	α_1 [–]	β_1 [–]
10.00	0.99_9	0.98	−3.48	0.85
μ_2 [MPa]	N_2 [–]	n_2 [–]	α_2 [–]	β_2 [–]
4.84	0.99_7	0.96	1.04	5.05

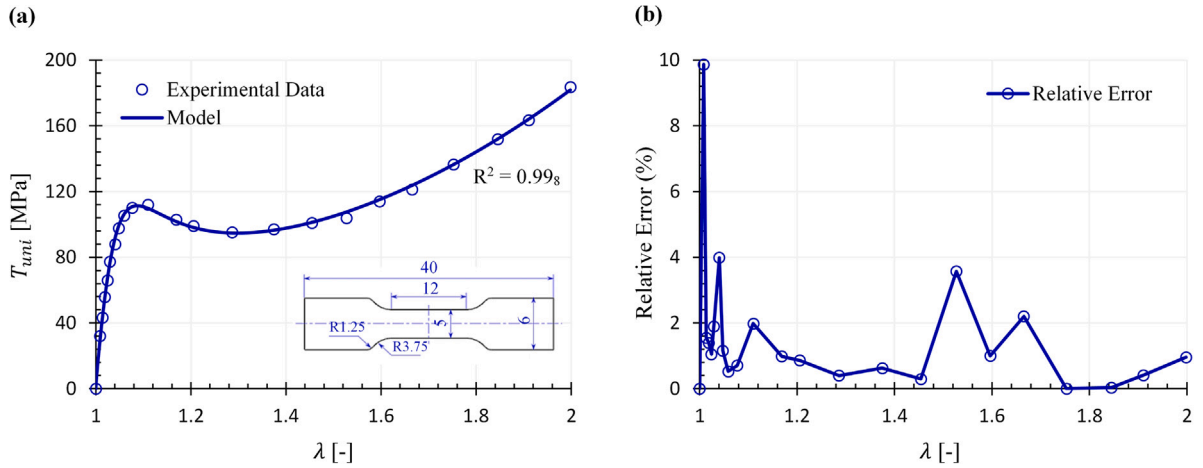

Fig. 3. Modelling results for the poly(methyl methacrylate) specimen of Ames et al. (2009), as reported in Uchida et al. (2022): (a) the fitting of the one-term expansion of the model with the data; and (b) the ensuing relative errors. The inset in panel (a) schematically represents the geometry and dimensions (in mm) of the specimens (adopted from Uchida et al. (2022) with permission).

Table 2
The identified model parameter values for the elastic and inelastic behaviour of the poly(methyl methacrylate) specimen due to Ames et al. (2009), on using the one-term expansion of the proposed model.

μ [MPa]	N [–]	n [–]	α [–]	β [–]
1.29_5	0.93	0.17	−7.48	0.79

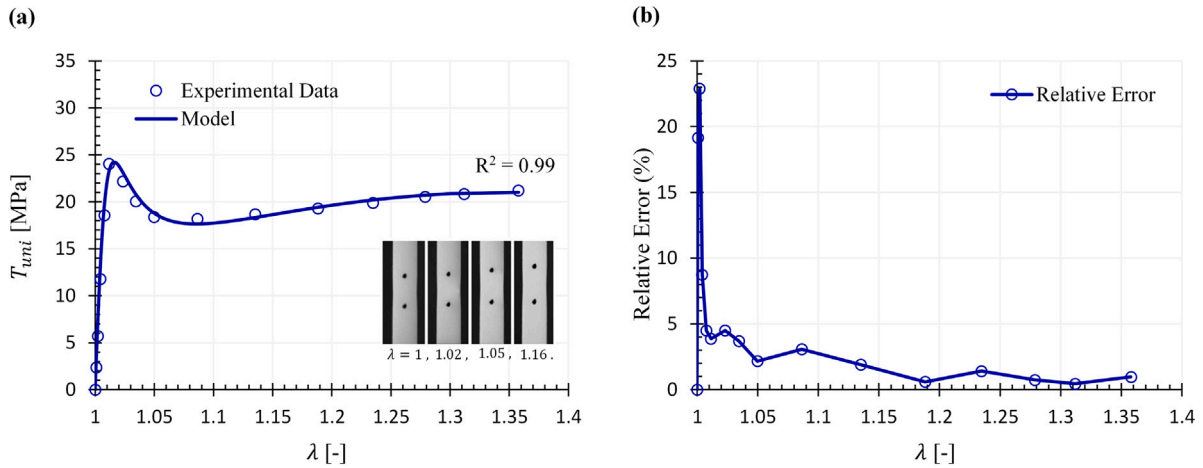

Fig. 4. Modelling results for high-impact polystyrene samples under uniaxial deformation at ambient temperature due to G'Sell et al. (2002): (a) the fitting of the two-term expansion of the model with the data; and (b) the ensuing relative errors. The inset represents the typical deformation of the samples at various levels of λ (adapted from G'Sell et al. (2002) with permission).

Table 3
Model parameter values for the large elastic and inelastic deformation of high-impact polystyrene samples of G'Sell et al. (2002) under uniaxial tension.

μ_1 [MPa]	N_1 [–]	n_1 [–]	α_1 [–]	β_1 [–]
2.61	0.99_8	0.93	−7.01	0.99
μ_2 [MPa]	N_2 [–]	n_2 [–]	α_2 [–]	β_2 [–]
5.82	9.76	0.09_8	−4.05	0.98

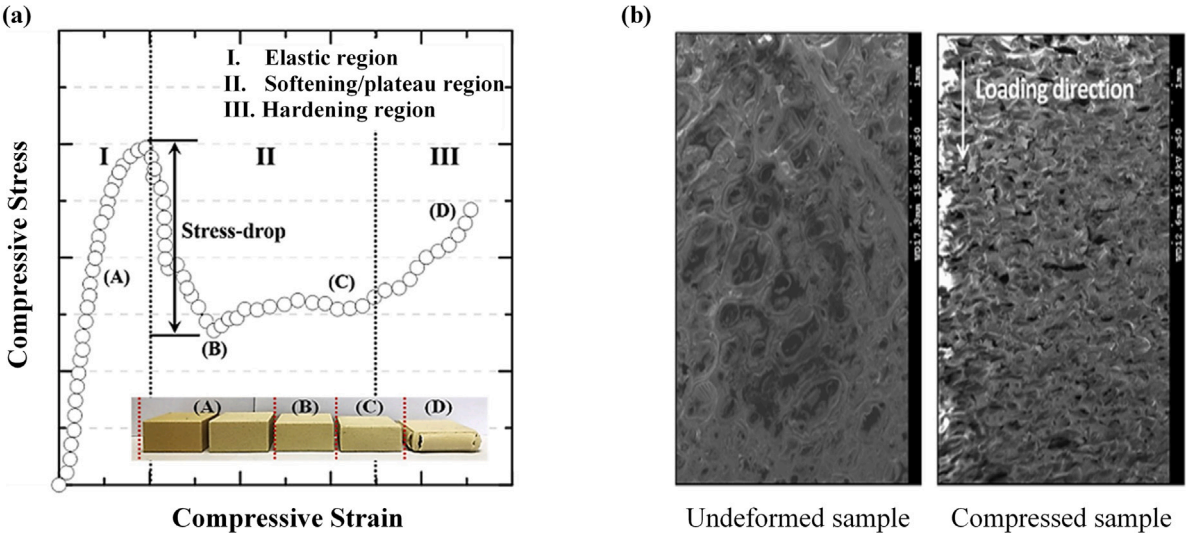

Fig. 5. (a) Schematic correlation of different stages of stress – strain curve with the compressive deformation of a closed-cell polyurethane foam specimen; and (b) SEM images of the microstructure of the foam before and after compression, highlighting the crushing of the voids.
Source: Images adapted from Lee et al. (2020) with permission.

Table 4
The identified model parameter values for the elastic and inelastic behaviour of polymeric foam specimens due to Lee et al. (2020).

Closed-cell polyurethane				
μ_1 [MPa]	N_1 [–]	n_1 [–]	α_1 [–]	β_1 [–]
10.00	0.99_9	0.91_5	−0.16	10.00
μ_2 [MPa]	N_2 [–]	n_2 [–]	α_2 [–]	β_2 [–]
2.96	0.98	0.56	1.29	1.20
μ_3 [MPa]	N_3 [–]	n_3 [–]	α_3 [–]	β_3 [–]
3.64	0.99_5	6.33	−0.91	3.53
Closed-cell polystyrene				
μ_1 [MPa]	N_1 [–]	n_1 [–]	α_1 [–]	β_1 [–]
0.17	0.99_8	0.99_6	1.25	4.37
μ_2 [MPa]	N_2 [–]	n_2 [–]	α_2 [–]	β_2 [–]
8.57	0.31	0.59	0.25_5	3.05
Open-cell polyurethane				
μ [MPa]	N [–]	n [–]	α [–]	β [–]
2.07	0.18	5.83	−1.09	0.92

3.3. Polymer foams

Following the example considered in Part I, here too I examine the application of the proposed model $W(\mathbf{F})$ in Eq. (1) to the uniaxial (compression) deformation of polymer foams via the dataset of Lee et al. (2020), encompassing open- and closed-cell polyurethane and closed-cell polystyrene specimens. The schematic in Fig. 5 illustrates the various stages of the deformation of a closed-cell polyurethane foam specimen in their study, correlated with various phases of the stress – deformation curve. The scanning electron microscopy (SEM) image of the microstructure of a specimen has also been reproduced in Fig. 5b, visually demonstrating that the size of the internal voids (or cells) decreases with increase in compression, resulting in a reduction in the void volume fraction of the specimens.

Complementing the previously considered examples, this dataset provides a good basis for evaluating the suitability and capability of the model for application to compressive deformation ranges; an attribute for which most of the existing models in the literature remain untested. Three-term, two-term and one-term expansions of the model were empirically observed to provide favourable fits to the deformation of closed-cell polyurethane, closed-cell polystyrene and open-cell polyurethane foam specimens, respectively. Table 4 lists the identified model parameter values for each specimen, and Fig. 6 demonstrates the fitting results. The tabulated numerical datapoints of this dataset have been provided in Part I. Compared with the modelling results in Part I, except for the closed-cell polyurethane sample, the proposed model in this work provides improved fits to the data, with a reduced number of

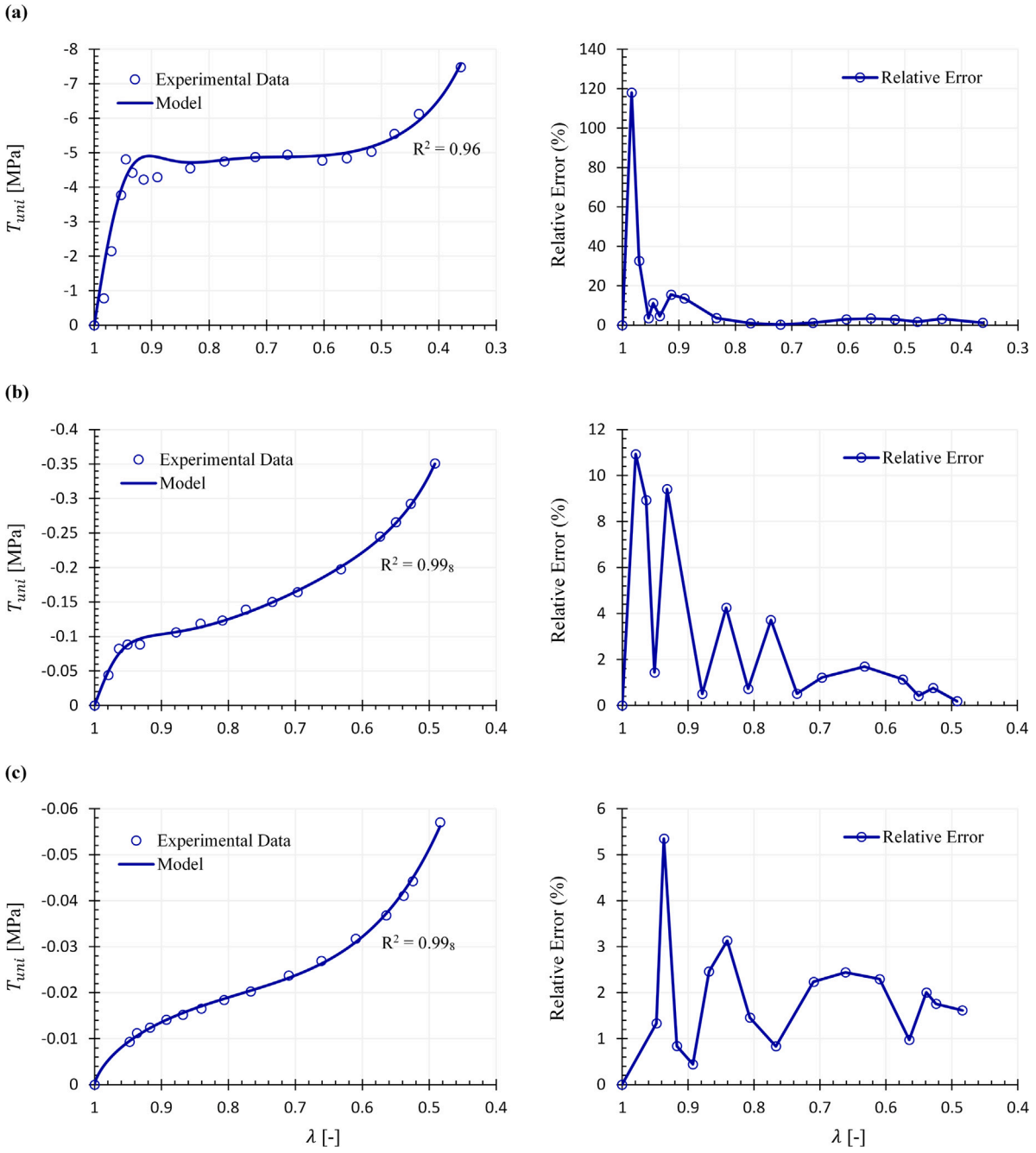

Fig. 6. Modelling results of the elastic and inelastic behaviours of polymeric foam specimens due to Lee et al. (2020) under uniaxial compression: (a) closed-cell polyurethane; (b) closed-cell polystyrene; and (c) open-cell polyurethane foams. The panels on the right-hand side present the relative errors. Note that the scale of the coordinate axes in the panels are different for a better clarity of presentation.

model parameters in like-for-like expansions of the models. For the closed-cell polyurethane specimens, the less favourable quality of fit than that of Part I is observed, even with the higher number of model parameters here (15) compared with that (12) of Part I.

3.4. Hydrogels

The quadruple-network hydrogel specimens of Vernerey et al. (2018) under uniaxial tension are considered here as an exemplar dataset for the application of the proposed model to the large deformation of multi-network hydrogels. As highlighted in Part I, this dataset presents a more complex behaviour than the classical double- or triple-network hydrogels, in that the specimens show a rapid initial nonlinear hardening up to a peak stress, followed by a drop in the stress and a plateau, indicative of a softening

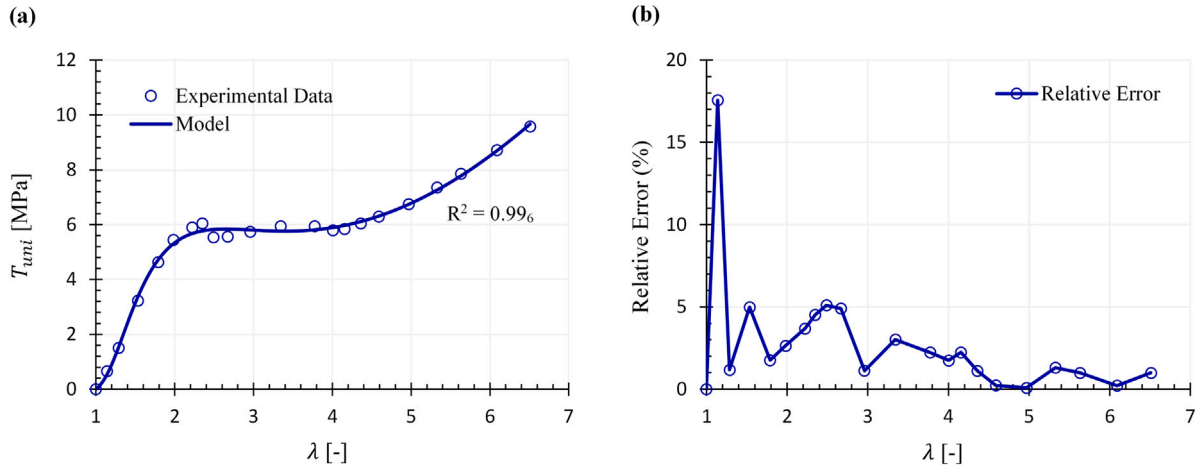

Fig. 7. Modelling results for the uniaxial tension of the quadruple-network hydrogel samples due to Vernerey et al. (2018): (a) the fitting of the three-term expansion of the model with the data; and (b) the ensuing relative errors.

Table 5
Model parameter values for the deformation behaviour of the quadruple-network hydrogel specimens of Vernerey et al. (2018), on using the three-term expansion of the model.

μ_1 [MPa]	N_1 [–]	n_1 [–]	α_1 [–]	β_1 [–]
2.49	0.97	0.43	−0.39	2.98
μ_2 [MPa]	N_2 [–]	n_2 [–]	α_2 [–]	β_2 [–]
3.85	3.89	0.47	−0.63	2.89
μ_3 [MPa]	N_3 [–]	n_3 [–]	α_3 [–]	β_3 [–]
2.22	0.90	10.00	−1.26	1.17

behaviour, proceeded by a final hardening phase. A three-term expansion of the model; i.e., $(i = 1, 2, 3)$ in Eq. (9), was deemed suitable for application to this dataset. Accordingly, the modelling results are shown in the plots of Fig. 7, and the obtained model parameter values are given in Table 5. The fitting results indicate the favourable application of the model to this dataset, with an R^2 value in excess of 0.99. However, compared with the two-term expansion of the binomial model in Part I, the ensuing relative errors appear higher. Note that the numerical values of the dataset by Vernerey et al. (2018) have been tabulated and presented in Part I.

3.5. Liquid crystal elastomers

The final example I wish to present here is due to the uniaxial deformation of isotropic-genesis polydomain LCEs, reported by Tokumoto et al. (2021). Isotropic-genesis polydomain LCEs possess macroscopically isotropic mechanical characteristics; however, with higher levels of deformation the microstructure may gradually reorganise itself into a monodomain configuration, as the mesogens become aligned with the director (e.g., see the schematic at the bottom of Fig. 8). Of particular interest in this dataset here is the 'soft elasticity' plateau in the stress – deformation curve of these specimens, which occurs within the polydomain phase, and provides a challenge to the models portending to capture this behaviour. The one-term expansion of the $W(\mathbf{F})$ model was fitted to this dataset, and the modelling results are illustrated in Fig. 8. Table 6 contains the identified model parameter values. The plots indicate the successful application of the model in capturing the uniaxial behaviour of these specimens, with R^2 values in excess of 0.99. Compared with the results in Part I, the presented model here provides as favourable a fit as the model therein, with one less model parameter (5 parameters here versus that of 6 in Part I). The tabulated numerical datapoints for this dataset have been provided in Anssari-Benam (2024a).

Table 6
The obtained model parameter values for the uniaxial deformation of polydomain LCE samples due to Tokumoto et al. (2021), on using the one-term expansion of the proposed model.

μ [kPa]	N [–]	n [–]	α [–]	β [–]
39.85	0.99	0.98	-1.24_5	2.35

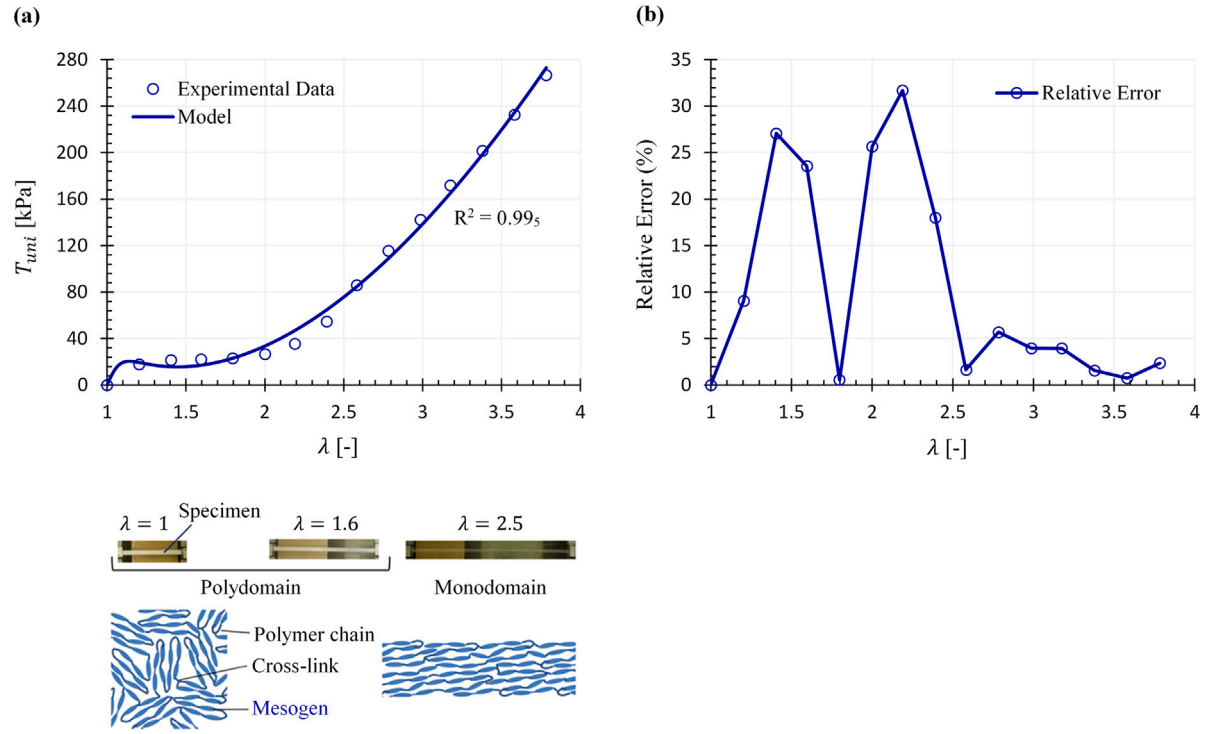

Fig. 8. Modelling results for the uniaxial tensile deformation of the polydomain LCE specimens of Tokumoto et al. (2021): (a) the fit obtained on using the one-term form of the model; and (b) the ensuing relative errors. The schematic at the bottom of panel (a) represents the microstructural reorganisation of the chains and mesogens with increase in the level of deformation.
Source: Adapted from Tokumoto et al. (2021) with permission.

4. Incorporation of other inelastic effects

In large deformation of polymers, occasions may frequently arise where the inelastic behaviour of the subject specimen is further affected and exacerbated by factors other than the mere deformation gradient. These additional factors may include, but are not limited to, for example the rate of deformation (e.g., Uchida et al., 2022; Pan et al., 2024), the ambient/functioning temperature (e.g., Richeton et al., 2006; Abdel-Wahab et al., 2017), time-dependent effects and ageing (e.g., Dinari et al., 2021; Makki et al., 2023), level of crystallinity (e.g., Yan et al., 2021; Ayoub et al., 2024) etc. The *core hyperinelastic* deformation energy function $W(\mathbf{F})$ in Eq. (1) successfully, at least to a favourable degree, addresses the *deformation-induced* inelastic behaviour of polymers/elastomers, as exemplified by the datasets considered in Section 3. To incorporate these additional inelastic features, the $W(\mathbf{F})$ model may be augmented, in a thermodynamically consistent manner, to capture the inelastic behaviour(s) induced by those factors.

Towards this end, in this section a generalised modelling framework will be presented, with the central assumption that the model parameters of the *core hyperinelastic* deformation energy function $W(\mathbf{F})$ may evolve with; i.e., be a function of, the additional parameter of interest which gives rise to inelasticity. This framework is a generalisation[5] of the modelling approach originally put forward by Anssari-Benam and Hossain (2023), which was specific to only incorporating the rate of deformation into the basic hyperelastic strain energy function. Here, focus will be restricted to non-thermal features; i.e., only isothermal deformations are considered. Specifically, the specialisation of the general modelling framework for the incorporation of deformation rate, crystallinity ratio and the 3D printing angle will be pursued and presented here, followed by the application of the *augmented* model to extant datasets with regard to the effects of those features on the inelastic behaviour of subject polymer specimens.

4.1. A general framework for augmenting the core hyperinelastic function

Let us consider a general feature of interest, denoted by ξ, that gives rise to the inelastic behaviour of a subject polymer specimen aside from the deformation gradient $\mathbf{F}$. This feature ξ may belong to a tensorial or a scalar field, such as the deformation rate tensor

[5] I am grateful to an anonymous reviewer of a preceding work (Anssari-Benam and Saccomandi, 2024b), who shared with me the insight of generalising the approach of incorporating the rate-effects, so that a generic variable of interest could instead be considered.

or the temperature, respectively; though we remain mindful that in general scalars are indeed a subset of tensors, of rank zero. Hence, here we adopt the bold typeset notation for $\boldsymbol{\xi}$ to represent the general case, while noticing that for the special case of a scalar the normal typeset notation may be substituted.

The crux of the modelling framework postulated here is that the model parameters of the *core hyperinelastic* deformation energy function $W(\mathbf{F})$ may be considered to vary, i.e., evolve, with $\boldsymbol{\xi}$. Let us call the resulting function an *augmented hyperinelastic* function, denoted by $W^{\star}$:

$$W^{\star} \equiv W(\mathbf{F}, \boldsymbol{\xi}). \tag{10}$$

The dependence of $W^{\star}$ on $\mathbf{F}$ is understood via either the principal invariants I_j or the principal stretches λ_j, $j = 1, 2, 3$; while the dependence of $W^{\star}$ on $\boldsymbol{\xi}$ may be through a specifically defined *scalar* measure of $\boldsymbol{\xi}$.

The said *scalar* measure of $\boldsymbol{\xi}$ may be defined as follows. Let $\mathbf{a}$ define a vectoral information of interest on $\boldsymbol{\xi}$, say, the direction of exertion or effect etc of $\boldsymbol{\xi}$, as:

$$\mathbf{a} = \left[\delta_1, \delta_2, \delta_3\right]^{\mathrm{T}}, \quad \delta_j = \begin{cases} 1, & \text{if } j \text{ is the direction of interest}, \\ 0, & \text{otherwise}. \end{cases} \tag{11}$$

Now let tensor $\mathbf{A}$ be constructed from $\mathbf{a}$ via:

$$\mathbf{A} = \mathbf{a} \otimes \mathbf{a}, \tag{12}$$

where $\otimes$ denotes the dyadic operator. The *scalar* measure of interest of $\boldsymbol{\xi}$, denoted by ζ, may then be considered as an array of interest in matrix $\mathbf{B}$, defined by:

$$\mathbf{B} = \mathbf{A}\,\boldsymbol{\xi}, \quad \zeta = \text{Array of interest}\,(\mathbf{B}). \tag{13}$$

This 'array of interest' may, for example, be the array with the maximum or minimum value of $\mathbf{B}$ etc, depending on the significance of the physical representation of the arrays of $\mathbf{B}$, and/or the intended modelling application.

Remark 1. Note that when ξ is a scalar (and hence why the normal typesetting font), say the crystallinity ratio, it is clear that $\mathbf{a}$ and $\mathbf{A}$ both become scalars, with the value of 1; i.e., $a = A = 1$, and as such the scalar measure of interest ζ becomes equal to the scalar value ξ. For most applications, such as those that will be seen in the sequel, this is a convenient result. However, should other scalar measures/factors of ξ be required in some applications, Eq. (13) provides the flexibility to define ζ in any manner that may be desired.

With ζ and $W^{\star}$ so defined, given by Eqs. (10) and $(13)_2$, respectively, we may now proceed to devising the 'augmented' modelling framework. We define a free energy function $\widetilde{W}^{\star}$ as:

$$\widetilde{W}^{\star} = W^{\star} - w(\boldsymbol{\xi}), \tag{14}$$

where w is an auxiliary function, only a function of $\boldsymbol{\xi}$, which readily results in:

$$\frac{\partial w(\boldsymbol{\xi})}{\partial \mathbf{F}} = \mathbf{0}. \tag{15}$$

The dependence of w on $\boldsymbol{\xi}$ is considered via the same defined measure of interest ζ in Eq. $(13)_2$; though the exact functional form of this dependency need not be specified, as it will not enter the stress – deformation relationships due to Eq. (15). For thermodynamical consistency, however, as will be demonstrated in the next section, we impose the following condition on w:

$$\frac{\partial w(\boldsymbol{\xi})}{\partial \boldsymbol{\xi}} = \frac{\partial W(\mathbf{F}, \boldsymbol{\xi})}{\partial \boldsymbol{\xi}}. \tag{16}$$

On using Eqs. (1), (10) and $(13)_2$, the specialised functional form of the *augmented hyperinelastic* function $W^{\star}$ can now be expressed as:

$$W^{\star} \equiv W(\mathbf{F}, \boldsymbol{\xi}) = W\left(\lambda_1, \lambda_2, \lambda_3, \zeta\right) = \sum_{i=1} \frac{3\left[\eta_i(\zeta) - 1\right]}{2\eta_i(\zeta)} \Omega_i(\zeta)\, \phi_i(\zeta) \left\{ \frac{1}{3\phi_i(\zeta)\left[\eta_i(\zeta) - 1\right]} \left(\lambda_1^{\kappa_i(\zeta)} + \lambda_2^{\kappa_i(\zeta)} + \lambda_3^{\kappa_i(\zeta)} - 3\right)^{\Gamma_i(\zeta)} \right. \tag{17}$$

$$\left. - \ln\left(\frac{\lambda_1^{\kappa_i(\zeta)} + \lambda_2^{\kappa_i(\zeta)} + \lambda_3^{\kappa_i(\zeta)} - 3\phi_i(\zeta)}{3 - 3\phi_i(\zeta)} \right)^{\Gamma_i(\zeta)} \right\},$$

with $\lambda_1\lambda_2\lambda_3 = 1$ due to incompressibility, and where:

$$\mu_i \equiv \Omega_i(\zeta), \quad N_i \equiv \phi_i(\zeta), \quad n_i \equiv \eta_i(\zeta), \quad \alpha_i \equiv \kappa_i(\zeta), \quad \beta_i \equiv \Gamma_i(\zeta). \tag{18}$$

Note that Ω_i, ϕ_i, η_i, κ_i and Γ_i are, as yet, unspecified scalar functions of ζ, whose exact functional forms may be designated empirically.

The final step is to derive and present the ensuing stress – deformation relationships using the devised *augmented hyperinelastic* function $W^\star$. Since, as we will see in Section 4.3, the considered datasets all report the inelastic behaviour of the subject specimens under uniaxial deformation, it suffices for the purpose of this work to only focus on the $T_{uni} - \lambda$ relationship. Accordingly, using the representation formula in Eq. (8), and subject to the assumption of plane stress $\left(T_{33}=0\right)$, we obtain:

$$T_{uni}=\sum_{i=1}\frac{\Omega_i\left(\zeta\right)\kappa_i\left(\zeta\right)\Gamma_i\left(\zeta\right)}{2\eta_i\left(\zeta\right)}\frac{\left[\lambda^{\kappa_i(\zeta)}+2\lambda^{-0.5\kappa_i(\zeta)}-3\right]^{\Gamma_i(\zeta)1}\left[\lambda^{\kappa_i(\zeta)}+2\lambda^{-0.5\kappa_i(\zeta)}\;3\phi_i\left(\zeta\right)\right]\;3\phi_i\left(\zeta\right)\left[\eta_i\left(\zeta\right)-1\right]}{\lambda^{\kappa_i(\zeta)}+2\lambda^{-0.5\kappa_i(\zeta)}\;3\phi_i\left(\zeta\right)}\times\left[\lambda^{\kappa_i(\zeta)}-\frac{1}{\lambda^{0.5\kappa_i(\zeta)}}\right]. \tag{19}$$

The explicit functional forms of Ω_i, ϕ_i, η_i, κ_i and Γ_i will be formulated in Section 4.3, for application to the inelastic behaviour of each subject specimen and dataset.

4.2. Thermodynamics consistency

The demonstration of the thermodynamical consistency of the proposed generalised modelling framework in Section 4.1 is similar to that presented in Part I. However, in the interest of completeness, I will recast the demonstration here too. Discounting the thermal effects,[6] the Clausius-Duhem inequality for the mechanical contributions reads (Holzapfel, 2000):

$$\mathcal{D}:=\frac{1}{2}\mathbf{S}:\dot{\mathbf{C}}-\dot{\mathcal{W}}\geq 0, \tag{20}$$

where $\mathcal{D}$ is the rate of dissipation per unit volume, $\mathcal{W}$ is the *free* energy, $\dot{\mathcal{W}}$ is its time derivative, $\mathbf{S}$ and $\dot{\mathbf{C}}$ are the 2nd Piola–Kirchhoff and the time-derivative of the right Cauchy–Green tensors, respectively, and the operator $(:)$ is 'double contraction'. The free energy of concern in the current modelling framework was defined in Section 4.1, via Eq. (14), as $\widetilde{W}^\star$. By substituting for $\mathcal{W}$ in the Clausius-Duhem inequality of Eq. (20) from Eq. (14) we get:

$$\mathcal{D}:=\frac{1}{2}\mathbf{S}:\dot{\mathbf{C}}-\dot{\widetilde{W}}^\star\geq 0\implies\mathcal{D}:=\frac{1}{2}\mathbf{S}:\dot{\mathbf{C}}-\left(\dot{W}^\star-\dot{w}\right)\geq 0. \tag{21}$$

where, for simplicity, we have dropped the notation for functional dependencies of $W^\star$ and w. On using the chain rule we find:

$$\dot{W}^\star=\frac{\mathrm{d}W^\star}{\mathrm{d}t}=\frac{\partial W^\star}{\partial\mathbf{C}}:\frac{\partial\mathbf{C}}{\partial t}+\frac{\partial W^\star}{\partial\boldsymbol{\xi}}:\frac{\partial\boldsymbol{\xi}}{\partial t}, \tag{22}$$

and:

$$\dot{w}=\frac{\mathrm{d}w}{\mathrm{d}t}=\frac{\partial w}{\partial\boldsymbol{\xi}}:\frac{\partial\boldsymbol{\xi}}{\partial t}, \tag{23}$$

which, in view of the condition in Eq. (16), may be written as:

$$\dot{w}=\frac{\partial W}{\partial\boldsymbol{\xi}}:\frac{\partial\boldsymbol{\xi}}{\partial t}. \tag{24}$$

Substituting Eqs. (22) and (24) into (21), and bearing in mind Eq. (10), results the following ansatz:

$$\mathcal{D}=\frac{1}{2}\mathbf{S}:\dot{\mathbf{C}}-\left(\frac{\partial W^\star}{\partial\mathbf{C}}:\dot{\mathbf{C}}\right)\geq 0. \tag{25}$$

Since the stress $\mathbf{S}$ must, by definition, be derived from the free energy $\widetilde{W}^\star$, and since w does not contribute to the computation of stress due to Eq. (15), we axiomatically have:

$$\mathbf{S}=2\frac{\partial W^\star}{\partial\mathbf{C}}, \tag{26}$$

which posits the relationship in Eq. (25) *a priori* satisfied.

4.3. Application to experimental data

The modelling framework devised in Section 4.1 considers a generic $\boldsymbol{\xi}$, and thereby ζ, as an arbitrary factor giving rise to an inelastic behaviour. In this section three diverse inelastic features $\boldsymbol{\xi}$ will be considered: deformation rate by way of exemplifying a tensorial $\boldsymbol{\xi}$, and crystallinity volume ratio and the printing angle (in additively manufactured (3D printed) polymer specimens) as representative examples of two scalar ξ factors. The relationships in Eqs. (13), (18), and thus (17) and (19), will be specialised for each of the aforementioned applications accordingly, and the ensuing *augmented hyperinelastic* model will be fitted with the experimental data to showcase the suitability and capability of the proposed modelling approach to capturing those inelastic effects.

[6] Recall that as in Part I, we are only concerned with isothermal deformations.

4.3.1. Modelling the effect of deformation rate

As per the practice in Section 3, here we consider a dataset that was also used in Part I, to provide the reader with a basis of comparison between the performance of the proposed model herein and that of Part I. In this regard, I start by modelling the effect of rate of deformation on the mechanical behaviour of open-cell polyurethane specimens of Lee et al. (2020). First, however, we shall need to specialise the specific functional forms of $\boldsymbol{\xi}$, ζ, and $W^{\star}$.

Accordingly, since we wish to consider the rate of deformation effects, and that $\dot{\lambda}_j$ are control variables in experiments; i.e., $\dot{\lambda}_j$ is set in rate-dependent experiments, it is natural to consider $\boldsymbol{\xi}$ as the tensor $\dot{\mathbf{F}}$:

$$\boldsymbol{\xi} \equiv \dot{\mathbf{F}}. \tag{27}$$

Since Lee et al. (2020) consider uniaxial deformation (compression) in their experiments, say in direction $j = 1$, i.e., λ_1, we find that $\mathbf{a} = [1, 0, 0]^{\mathrm{T}}$, and thus $\mathbf{A}$ becomes a matrix with $A_{11} = 1$ and all other arrays zero. It follows that:

$$\mathbf{B} = \mathbf{A}\,\dot{\mathbf{F}}. \tag{28}$$

Following Anssari-Benam and Hossain (2023), we choose the 'array of interest' of $\mathbf{B}$ to be the array whose absolute value is the maximum value of all arrays; i.e.,

$$\zeta = \max\left\{\left|\mathbf{A}\,\dot{\mathbf{F}}\right|\right\}, \tag{29}$$

which, in this case, is equivalent to the absolute value of the corresponding component of $\dot{\lambda}_1$:

$$\zeta = \max\left\{\left|\mathbf{A}\,\dot{\mathbf{F}}\right|\right\} = \left|\dot{\lambda}_1\right|. \tag{30}$$

Next step is to specialise the functional form of $W^{\star}$, whose generic form has been given by Eq. (17). To do so, one needs to first designate the functional forms of $\Omega_i(\zeta)$, $\phi_i(\zeta)$, $\eta_i(\zeta)$, $\kappa_i(\zeta)$ and $\Gamma_i(\zeta)$. The choice for these functional dependencies is, essentially, an empirical decision, judged by how well the ensuing model captures the rate-dependent behaviour, and balanced by the total number of parameters in the *augmented* model that will enter the process of fitting.

Perhaps the simplest form to consider is a linear dependency of the *core* model parameters on the (measure of) deformation rate, ζ. This choice has previously proved effective and versatile in capturing the rate-dependent behaviour of a variety of elastomers; see Anssari-Benam and Hossain (2024). In that spirit, I also choose a linear dependency of Ω_i, ϕ_i, η_i, κ_i and Γ_i on ζ, as:

$$\Omega_i(\zeta) = \mu_i + g_{1,i}\,\zeta, \quad \phi_i(\zeta) = N_i + g_{2,i}\,\zeta, \quad \eta_i(\zeta) = n_i + g_{3,i}\,\zeta, \quad \kappa_i(\zeta) = \alpha_i + g_{4,i}\,\zeta, \quad \Gamma_i(\zeta) = \beta_i + g_{5,i}\,\zeta, \tag{31}$$

where $g_{z,i} \in \mathbb{R}$, $z = 1, \ldots, 5$, are the added parameters of the *augmented* model, $g_{1,i}$ has units of [Pa s] and all other $g_{z,i}$ are dimensionless. The considered linear form in Eq. (31) has two advantages. First, it introduces the least amount of added parameters into the *augmented* model. And, second, at the limit of the quasi-static deformation, where $\zeta \to 0$, the *core* model parameters μ_i, N_i, n_i, α_i and β_i are readily recovered.

In Section 3.3, the quasi-static elastic and inelastic deformation behaviours of open-cell polyurethane specimens of Lee et al. (2020) were modelled using a one-term expansion of the *core* model; i.e., $i = 1$. We therefore opt for the one-term expansion of the *augmented hyperinelastic* model here as well. In addition, since the deformation in that dataset is uniaxial, we have: $\lambda_1 = \lambda$, $\lambda_2 = \lambda_3 = \lambda^{-0.5}$, and from Eq. (30)$\zeta = |\dot{\lambda}|$. Accordingly, the relationships in Eq. (31) simplify to:

$$\Omega(\zeta) = \mu + g_1\left|\dot{\lambda}\right|, \quad \phi(\zeta) = N + g_2\left|\dot{\lambda}\right|, \quad \eta(\zeta) = n + g_3\left|\dot{\lambda}\right|, \quad \kappa(\zeta) = \alpha + g_4\left|\dot{\lambda}\right|, \quad \Gamma(\zeta) = \beta + g_5\left|\dot{\lambda}\right|, \tag{32}$$

where, for simplicity, we have dropped the i indices.

Now, using the one-term expansion of the *augmented hyperinelastic* function in Eq. (19), i.e., $i = 1$, and the relationships in Eq. (32), we proceed with modelling the uniaxial rate-dependent data of Lee et al. (2020) on open-cell polyurethane specimens. Therein they provide, in addition to the quasi-static deformation data, the rate-dependent behaviour of the specimens under compressive deformation rates of $\left|\dot{\lambda}\right| = 0.08\ \mathrm{s}^{-1}$ and $4.6\ \mathrm{s}^{-1}$. Since the values of the *core* model parameters μ, N, n, α and β were identified in Section 3.3, under quasi-static deformation and given in Table 4, we keep those values in the *augmented* model fixed, and fit the one-term expansion of the *augmented hyperinelastic* model in Eq. (19) simultaneously to the two rate-dependent datasets. In this case, therefore, there are only five additional rate-dependent parameters to be optimised; namely g_z, $z = 1, \ldots, 5$. The modelling results are presented in Fig. 9, and Table 7 gives the obtained values of the rate parameters. The tabulated numerical datapoints for these datasets can be found in Part I. The model is seen to capture the rate-dependent behaviour of these specimens favourably, with R^2 values in excess of 0.99. With two model parameters less, the favourability of the modelling results here are comparable with that of the model in Part I.

The next dataset to consider here is on the rate-dependent behaviour of amorphous polylactic acid (PLA) specimens under compression, as reported by Pan et al. (2024). Cylindrical test samples of 4 mm height and 5 mm diameter were subjected to uniaxial compression deformations at quasi-static, $0.01\ \mathrm{s}^{-1}$ and $0.1\ \mathrm{s}^{-1}$ rates, at a constant temperature of 37 °C. The inelastic behaviour of these specimens was reported to be facilitated by shear banding, and therein they propose a model capable of capturing shear and craze yielding. Here, however, I use the deformation energy-based hyperinelastic approach devised in this work to capture the inelastic behaviour of these glassy polymers.

For this purpose, the two-term expansion of the *augmented* model in Eq. (19); i.e., $i = 1, 2$, is used. Given the intricate non-monotonic stress – deformation behaviour of the specimens (see Fig. 10), it was empirically observed that a linear dependency of the *core* model parameters on $\dot{\lambda}$ does not accurately capture the rate-dependent behaviour of the samples. Following Anssari-Benam

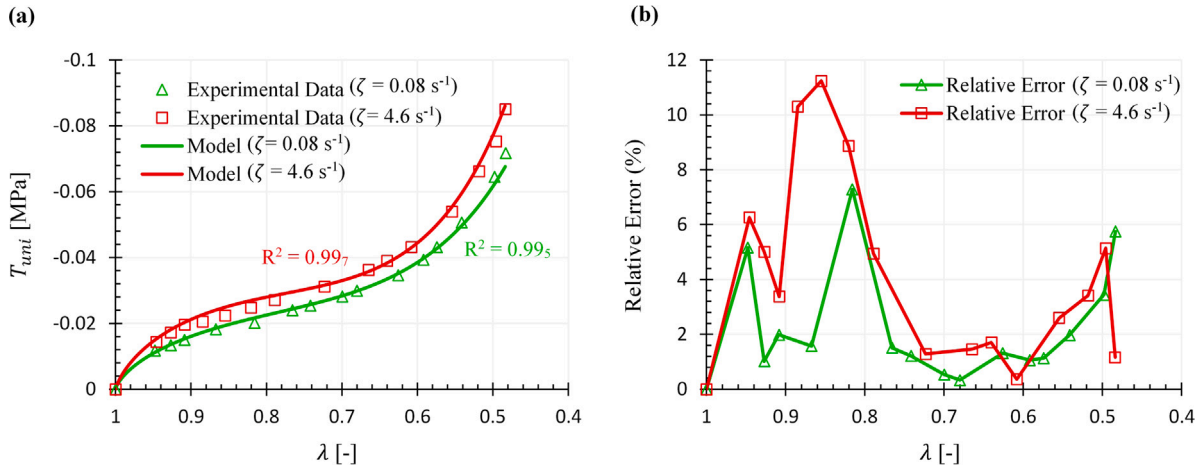

Fig. 9. Modelling results for the rate-dependent behaviour of open-cell polyurethane specimens due to Lee et al. (2020) under uniaxial compression at two deformation rates, using the one-term expansion of the model in Eq. (19): (a) fitting with the data; and (b) the resulting relative error plots. See the online version for plots in colour.

Table 7
The identified values of the rate-dependent parameters g_z, $z = 1, \dots, 5$, when fitting the one-term expansion of the model in Eq. (19) to the rate-dependent behaviour of open-cell polyurethane specimens due to Lee et al. (2020). See Table 4 for the values of the *core* model parameters μ, N, n, α and β.

g_1 [MPa s]	g_2 [–]	g_3 [–]	g_4 [–]	g_5 [–]
4.82	0.00_1	0.00_3	0.08_5	0.01

and Saccomandi (2024a, 2024b), where exponential forms of dependency on the deformation rate have been advocated, a two-parameter skewed exponential dependency is chosen here to designate the functional forms of $\Omega_i(\zeta)$, $\phi_i(\zeta)$, $\eta_i(\zeta)$, $\kappa_i(\zeta)$ and $\Gamma_i(\zeta)$, as follows:

$$\begin{cases} \Omega_i(\zeta) = a_{1,i} + (\mu_i - a_{1,i}) \exp\left(|\dot{\lambda}|^{b_{1,i}}\right), \\ \phi_i(\zeta) = a_{2,i} + (N_i - a_{2,i}) \exp\left(|\dot{\lambda}|^{b_{2,i}}\right), \\ \eta_i(\zeta) = a_{3,i} + (n_i - a_{3,i}) \exp\left(|\dot{\lambda}|^{b_{3,i}}\right), \\ \kappa_i(\zeta) = a_{4,i} + (\alpha_i - a_{4,i}) \exp\left(|\dot{\lambda}|^{b_{4,i}}\right), \\ \Gamma_i(\zeta) = a_{5,i} + (\beta_i - a_{5,i}) \exp\left(|\dot{\lambda}|^{b_{5,i}}\right), \end{cases} \tag{33}$$

where, in general, $a_{z,i}, b_{z,i} \in \mathbb{R}$, $z = 1, \dots, 5$, parameters $a_{1,i}$ bear the dimension of stress [Pa], while all other $a_{z,i}$ and $b_{z,i}$ parameters are dimensionless. Note that in the limit of quasi-static loading, i.e., $\dot{\lambda} \to 0$, the *core* model parameters μ_i, N_i, n_i, α_i and β_i are recovered.

On using the two-term expansion of the *augmented* model in Eq. (19), and the specified functional dependencies of $\Omega_i(\zeta)$, $\phi_i(\zeta)$, $\eta_i(\zeta)$, $\kappa_i(\zeta)$ and $\Gamma_i(\zeta)$ as given by Eq. (33), the results for fitting of the model to the dataset of Pan et al. (2024) are shown in Fig. 10. Note that for this fitting, the rate-independent form of the (two-term) model in Eq. (9) was first fitted to the quasi-static data to ascertain the *core* model parameter values. Once those values were obtained, they were kept fixed in the *augmented* model; i.e., the two term expansion of Eq. (19) and the $\Omega_i(\zeta)$, $\phi_i(\zeta)$, $\eta_i(\zeta)$, $\kappa_i(\zeta)$ and $\Gamma_i(\zeta)$ functions given in Eq. (33), and the resulting *augmented* model was then simultaneously fitted to the 0.01 s^{-1} and 0.1 s^{-1} rate datasets. The measure of deformation in the original study by Pan et al. (2024) was taken as the true strain ε. However, the value of true strain for each datapoint was converted to stretch λ before the fitting process ($\varepsilon = \ln \lambda$). In keeping with the original data, the fitting results in Fig. 10 are also presented in true strain. The R^2 values for these fits are in excess of 0.94. The identified model parameter values are given in Table 8. The relative error plots for this fitting have been spared, due to the interference of many data points in the plot, as well as the lower values of R^2 which is already indicative of the deviation of the model form the data. The numerical values of the datapoints pertaining to this dataset have been tabulated and presented in Appendix, Table A.2.

It is interesting to note the obtained values of β_i in Table 8, as well as those of $a_{5,i}$ and $b_{5,i}$. It is observed that $\beta_i = 1$, $a_{5,i} = 1$ and $b_{5,i} = 0$, which renders the exponential term in Γ_i superfluous. This means that β_i can effectively be fixed to 1, and Γ_i does not vary with the rate of deformation. Therefore, these parameters can be taken out of the fitting process, rendering the overall number of

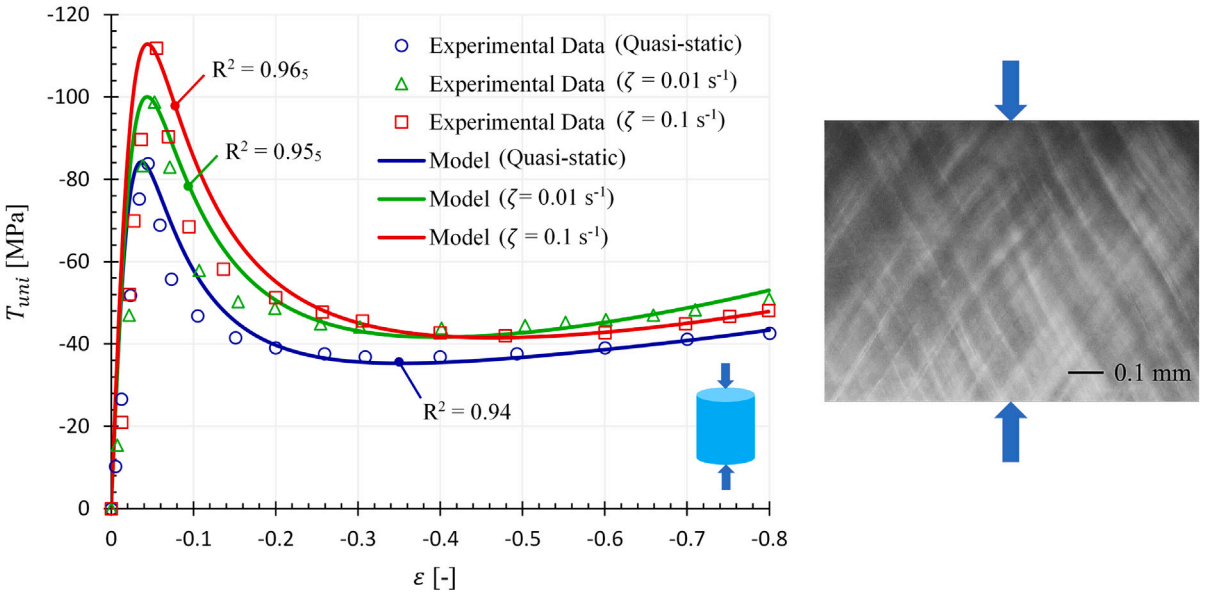

Fig. 10. Modelling results for the rate-dependent behaviour of amorphous polylactic acid (PLA) samples of Pan et al. (2024) under compression. A two-term expansion of the *augmented* model in Eq. (19), with a skewed exponential functional dependency of the model parameters on the deformation rate given by Eq. (33), was simultaneously fitted with the quasi-static and rate data. Note that the x axis represents the true strain, denoted by ε. The inset on the right is a micrograph from the centre of a specimen under compression, evidencing the occurrence of shear banding. The arrows indicate the direction of loading. See the online version for plots in colour (adopted from Pan et al. (2024) with permission).

Table 8
Obtained model parameter values for the rate-dependent behaviour of the amorphous polylactic acid (PLA) samples of Pan et al. (2024) under compression, using the two-term expansion of the *augmented* model in Eq. (19), with a skewed exponential functional dependency of the model parameters on the deformation rate, as given by Eq. (33).

Core model parameters				
μ_1 [MPa]	N_1 [–]	n_1 [–]	α_1 [–]	β_1 [–]
0.62	0.99_6	0.23	3.41	1
μ_2 [MPa]	N_2 [–]	n_2 [–]	α_2 [–]	β_2 [–]
4.20	0.99_8	0.27	0.07_5	1
Rate parameters				
$a_{1,1}$ [MPa]	$a_{2,1}$ [–]	$a_{3,1}$ [–]	$a_{4,1}$ [–]	$a_{5,1}$ [–]
−22.31	0.99	−0.18	5.01	1
$b_{1,1}$ [MPa]	$b_{2,1}$ [–]	$b_{3,1}$ [–]	$b_{4,1}$ [–]	$b_{5,1}$ [–]
0.25	0.27	0.04	0.16	0
$a_{1,1}$ [MPa]	$a_{2,2}$ [–]	$a_{3,2}$ [–]	$a_{4,2}$ [–]	$a_{5,2}$ [–]
−50.52	4.80	7.55	0.17	1
$b_{1,1}$ [MPa]	$b_{2,2}$ [–]	$b_{3,2}$ [–]	$b_{4,2}$ [–]	$b_{5,2}$ [–]
1.94	1.61	1.95	0.37	0

parameters in the *augmented* model equal to 24 (8 *core* parameters and 16 rate-dependent parameters). This total number of model parameters is rather high; however, the improved quality of fits compared with the model in the original study of Pan et al. (2024), with comparable number of model parameters, is noticeable.

4.3.2. *Modelling the effect of crystallinity volume*

The large deformation behaviour of semi-crystalline polyethylene specimens is known to depend on, amongst other factors, the crystallinity index; i.e., the volume ratio of crystallinity v_c, of the subject system (see, e.g., the contributions by Zaïri and co-workers including (Ayoub et al., 2011), Abdul-Hameed et al. (2014) and Yan et al. (2021), *inter alia*). These semi-crystalline polyethylene

Table 9
Model parameter values for modelling the effect of crystallinity ratio ν_c on the deformation of semi-crystalline polyethylene samples due to Yan et al. (2021), under uniaxial tension. A two-term expansion of the *augmented* model in Eq. (19) was used, with a linear functional dependency of the model parameters on ν_c, as given by Eq. (35).

Core model parameters				
μ_1 [MPa]	N_1 [–]	n_1 [–]	α_1 [–]	β_1 [–]
0.72	0.82	0.68	−2.31	1.21
μ_2 [MPa]	N_2 [–]	n_2 [–]	α_2 [–]	β_2 [–]
10.00	0.22	12.70	0.92	0.80
Augmented model parameters				
$m_{1,1}$ [MPa]	$m_{2,1}$ [–]	$m_{3,1}$ [–]	$m_{4,1}$ [–]	$m_{5,1}$ [–]
13.30	0.29	0.42	1.28×10^{-8}	−0.79
$m_{1,2}$ [MPa]	$m_{2,2}$ [–]	$m_{3,2}$ [–]	$m_{4,2}$ [–]	$m_{5,2}$ [–]
−17.42	−0.38	-4.70_5	2.03	2.52_5

systems exhibit a nearly elastomeric behaviour at low crystallinity, while at higher crystallinity they transition to a thermoplastic-like behaviour ($0 < \nu_c < 1$). Without wishing to emphasise or undermine the importance of correlating these behaviours directly with the microstructure, a continuum-based model that can macroscopically capture the effect of the crystallinity ratio on the observed macro-level behaviour of the specimens would seem a useful modelling tool for the prediction of the performance of polyethylene-based parts.

This undertaking may be made possible on using the general modelling framework presented in Section 4.1, where ξ now is related to a scalar field, namely the crystallinity volume. It follows that **a** and **A** in Eqs. (11) and (12), respectively, become a scalar: $a = A = 1$, and matrix **B** in Eq. $(13)_1$ becomes equivalent to the scalar value of ξ. Accordingly, one may then take ζ in Eq. $(13)_2$ directly as the measure of crystallinity volume ratio, ν_c:

$$\zeta = \nu_c \,. \tag{34}$$

With this measure of ζ at hand, it only remains to ascribe an appropriate functional form to the dependency of the *core* model parameters on ζ, $\Omega_i(\zeta)$, $\phi_i(\zeta)$, $\eta_i(\zeta)$, $\kappa_i(\zeta)$ and $\Gamma_i(\zeta)$, as in Eq. (18). The so designated functions may be used to form the *augmented hyperinelastic* function $W^\star$ in Eq. (17), and subsequently the stress – deformation relationships may be derived accordingly; e.g., Eq. (19) for the case of uniaxial deformation.

To this end, we note the datasets of Abdul-Hameed et al. (2014) and Yan et al. (2021), which report on the large deformation of commercial polyethylene samples with three different crystallinity ratios; i.e., $\nu_c = 15.1\%$, 30% and 72.4%, including their behaviour under quasi-static uniaxial tension. On taking the sample with the lowest crystallinity ratio (15.1%) as the specimen with the base-line behaviour, let us empirically stipulate a linear functional dependency of $\Omega_i(\zeta)$, $\phi_i(\zeta)$, $\eta_i(\zeta)$, $\kappa_i(\zeta)$ and $\Gamma_i(\zeta)$ on ν_c, for consideration in the *augmented* model, in order to then fit the model to the datasets with varying crystallinity ratios. The specific functional forms $\Omega_i(\zeta)$, $\phi_i(\zeta)$, $\eta_i(\zeta)$, $\kappa_i(\zeta)$ and $\Gamma_i(\zeta)$ are considered to be:

$$\begin{cases} \Omega_i(\zeta) = m_{1,i}\left(\nu_c - \nu_{c_0}\right) + \mu_i \,, \\ \phi_i(\zeta) = m_{2,i}\left(\nu_c - \nu_{c_0}\right) + N_i \,, \\ \eta_i(\zeta) = m_{3,i}\left(\nu_c - \nu_{c_0}\right) + n_i \,, \\ \kappa_i(\zeta) = m_{4,i}\left(\nu_c - \nu_{c_0}\right) + \alpha_i \,, \\ \Gamma_i(\zeta) = m_{5,i}\left(\nu_c - \nu_{c_0}\right) + \beta_i \,, \end{cases} \tag{35}$$

where, in general, $m_{z,i} \in \mathbb{R}$, $z = 1, \ldots, 5$, $m_{1,i}$ have the dimension of stress [Pa] and all other $m_{z,i}$ are dimensionless. Note that ν_{c_0} is the value of the base-line crystallinity ratio, which in the case of the considered samples here is: $\nu_{c_0} = 0.151$. At the limit where $\nu_c = \nu_{c_0}$, the *core* model parameters μ_i, N_i, n_i, α_i and β_i are recovered.

To fit with the data, the deformation dataset pertaining to the base-line specimen was first fitted with the two-term expansion of the *core* model, in Eq. (9), to obtain the base-line model parameter values (i.e., the values of the *core* parameters μ_i, N_i, n_i, α_i and β_i). Once those values were obtained, they were kept fixed in the two-term expansion of the *augmented* model in Eq. (19), with the functional dependencies of $\Omega_i(\zeta)$, $\phi_i(\zeta)$, $\eta_i(\zeta)$, $\kappa_i(\zeta)$ and $\Gamma_i(\zeta)$ given by Eq. (35), which was simultaneously fitted with the remaining two datasets with varying crystallinity ν_c ratios. The modelling results, along with the relative error plots, are shown in Fig. 11, and Table 9 summarises the identified model parameter values. The model appears to capture favourably the classical elastomer-like behaviour of the specimens at the lowest crystallinity ratio (the plot in blue), as well as their thermoplastic-like behaviour at the highest crystallinity (the red plot). The R^2 values are in excess of 0.99. The tabulated numerical values of this dataset has been provide in Table A.3 of Appendix.

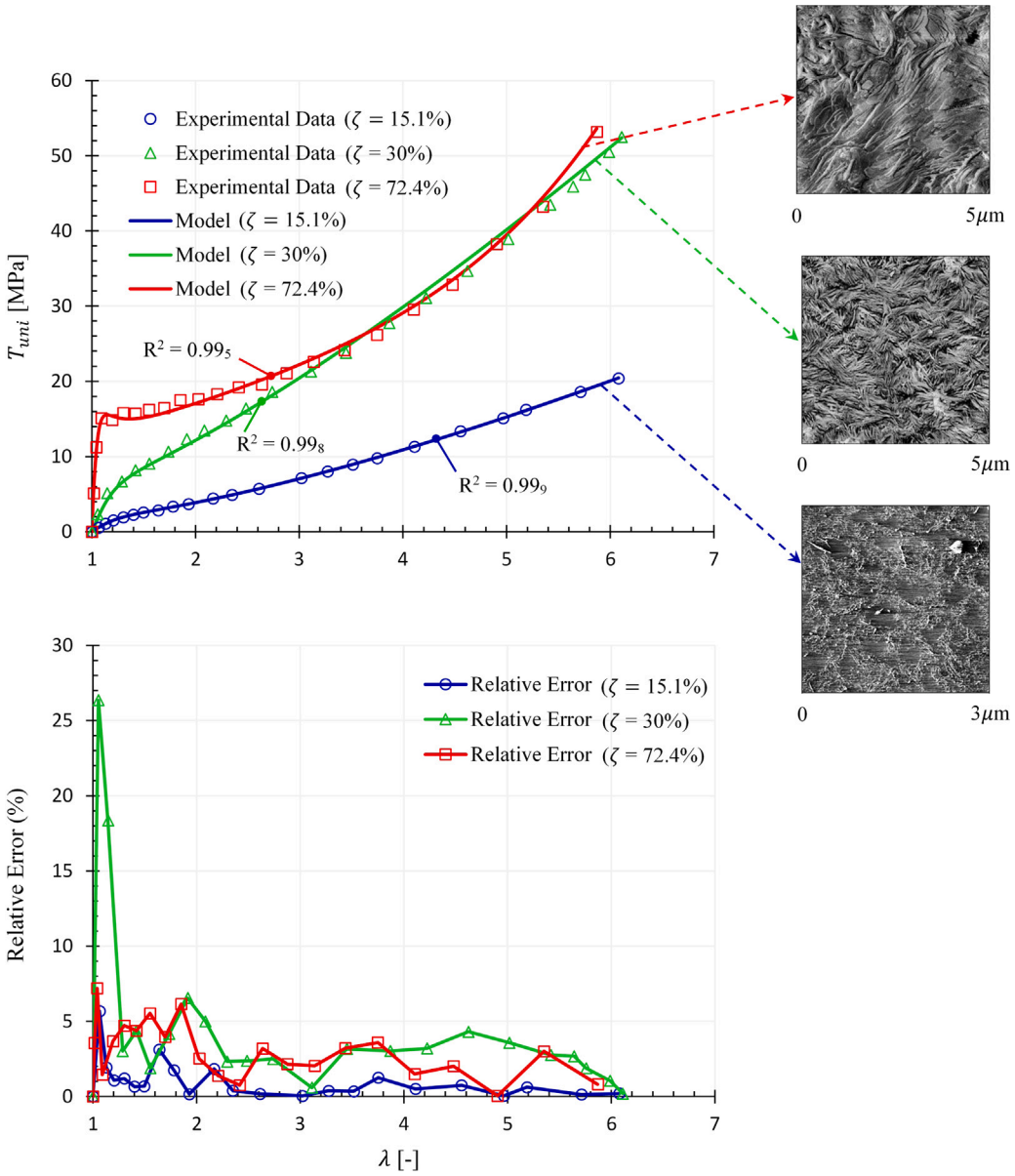

Fig. 11. Modelling the effect of change in crystallinity volume ratio on the large elastic and inelastic deformation of semi-crystalline polyethylene samples of Yan et al. (2021), originally reported in Abdul-Hameed et al. (2014), under uniaxial tension: (a) the fitting results; and (b) the ensuing relative error plots. The insets are AFM images, with different magnifications, of the samples' microstructure from Yan et al. (2021), showing isotropically distributed crystalline lamellae in samples with higher volumes of crystallinity (v_c = 30% and 72.4%), while fuzzy crystallites embedded in the amorphous matrix in the specimen with the lowest crystallinity ratio (v_c = 15.1%); courtesy of Prof. Fahmi Zaïri. See the online version for plots in colour.

4.3.3. Modelling the effect of 3D printing angle

There is experimental evidence in the literature which suggests that an additively manufactured 3D printed material may exhibit a differing mechanical behaviour than that of the same raw material (Li et al., 2020; Guo et al., 2024). In particular, the direction of the 3D printed specimen with regard to the printing bed appears to influence the mechanical behaviour of the final product (Sun et al., 2022; Guo et al., 2024). For such specimens, therefore, it appears valuable to have a robust modelling tool to simulate and *predict* the deformation behaviour of the final product, based on the orientation angle of 3D printing.

Accordingly, Guo et al. (2024) provide a detailed set of data on the uniaxial tensile deformation of 3D printed cylindrical dumbbell-shaped specimens, made of a curable photosensitive resin, printed at different angles with respect to the printing bed; at 0°, 30°, 45°, 60° and 90°. See the inset in Fig. 12a for a schematic. In light of the generalised modelling framework presented in Section 4.1, it is possible to model this angle-of −3D printing dependent behaviour using the devised *augmented hyperinelastic* model, where the *core* model parameters may be assumed to be a function of that angle; say θ.

Table 10
Modelling the effect of the 3D printing angle on the uniaxial tensile behaviour of additively manufactured specimens made from a curable photosensitive resin due to Guo et al. (2024), using the one-term expansion of the *augmented* model in Eq. (19), with the linear functional dependency of the model parameters on θ given by Eq. (35).

Core model parameters				
μ [MPa]	N [–]	n [–]	α [–]	β [–]
16.37_5	0.99	0.94_5	2.45	1.17_5
Augmented model parameters				
$u_{1,1}$ [MPa]	$u_{2,1}$ [–]	$u_{3,1}$ [–]	$u_{4,1}$ [–]	$u_{5,1}$ [–]
−5.08	-0.00_1	-0.00_6	0.13	−0.06

To do so, one must note that similar to the example of crystallinity ratio ν_c in the preceding section, the ξ variable of interest is related to a scalar field (and hence not in a bold typeset), dealing with the 3D printing angle (θ). Therefore, all the intermediary steps follow the same consequences as for the crystallinity ratio example, and one arrives at a scalar measure of ξ, namely ζ in Eq. $(13)_2$, as:

$$\zeta = \theta^\circ . \tag{36}$$

Again, the final step now is to specify the explicit functional forms of $\Omega_i(\zeta)$, $\phi_i(\zeta)$, $\eta_i(\zeta)$, $\kappa_i(\zeta)$ and $\Gamma_i(\zeta)$ in the *augmented* model; i.e., Eqs. (17) and (19), and designate the number of terms in the expansion of the model to acquire the best fit with the experimental data.

Consequently, in the interest of keeping the overall number of parameters in the *augmented* model to a minimum, the following linear functional dependency on the 3D printing bed angle is stipulated:

$$\begin{cases} \Omega_i(\zeta) = u_{1,i}\dfrac{\theta\,\pi}{180} + \mu_i\,, \\ \phi_i(\zeta) = u_{2,i}\dfrac{\theta\,\pi}{180} + N_i\,, \\ \eta_i(\zeta) = u_{3,i}\dfrac{\theta\,\pi}{180} + n_i\,, \\ \kappa_i(\zeta) = u_{4,i}\dfrac{\theta\,\pi}{180} + \alpha_i\,, \\ \Gamma_i(\zeta) = u_{5,i}\dfrac{\theta\,\pi}{180} + \beta_i\,, \end{cases} \tag{37}$$

where the $\frac{\pi}{180}$ multiplier is for converting the angle θ from degrees to its equivalent in radians. Similar to the previous applications, parameters $u_{z,i} \in \mathbb{R}$, $z = 1,\ldots,5$, $u_{1,i}$ have the dimension of stress [Pa] and all other $u_{z,i}$ are dimensionless. For the purpose of modelling the dataset of Guo et al. (2024), the one-term expansion of the model will be used.

Accordingly, the one-term expansion of the *augmented* model in Eq. (19); i.e., $i = 1$, and that of the relationships in Eq. (37) is fitted with the dataset. We take the deformation of the 3D specimen that has a 0° angle of orientation with the printing bed as the base-line behaviour. As such, the one-term expansion of the *core* model in Eq. (9) was first fitted with the deformation dataset of the base-line specimen (0°), to obtain the values of the *core* model parameters μ, N, n, α and β. Once those values were obtained, they were kept fixed in the one-term expansion of the *augmented* model in Eq. (19), where the functional forms of $\Omega(\zeta)$, $\phi(\zeta)$, $\eta(\zeta)$, $\kappa(\zeta)$ and $\Gamma(\zeta)$ are the one-term relationships (i.e., $i = 1$) of those given in Eq. (37), and the ensuing relationship of the *augmented* model was then simultaneously fitted with two datasets pertaining to the deformation of the specimens possessing 45° and 90° angles with the printing bed. The modelling results are presented in Fig. 12a, and the ensuing relative errors are provide in Fig. 12b. The model is seen to have captured the behaviours of the specimens favourably, with R^2 values in excess of 0.99. Table 10 contains the identified model parameter values. The tabulated numerical datapoints for this dataset have been given in Appendix, Table A.4.

To showcase the *predictive* capability of the *augmented* model, I undertook to *predict* the deformation behaviour of specimens that have 30° and 60° angles with the printing bed. That is, using the identified model parameter values in Table 10, the deformation behaviour of 30° and 60° specimens were *predicted*. The plots in Fig. 12c illustrate the correlation between the model predictions and the experimental data. The model appears proficient in predicting those behaviours.

5. Concluding remarks

Building on the foundations of the concept of *hyperinelasticity* presented in Part I, a generalised (principal) stretches-based model was formulated and presented here as the *core hyperinelastic* deformation energy function $W(\mathbf{F})$. The advantages of this model include lowering the number of constitutive model parameters, while maintaining a comprehensive 'universal' form from which many of

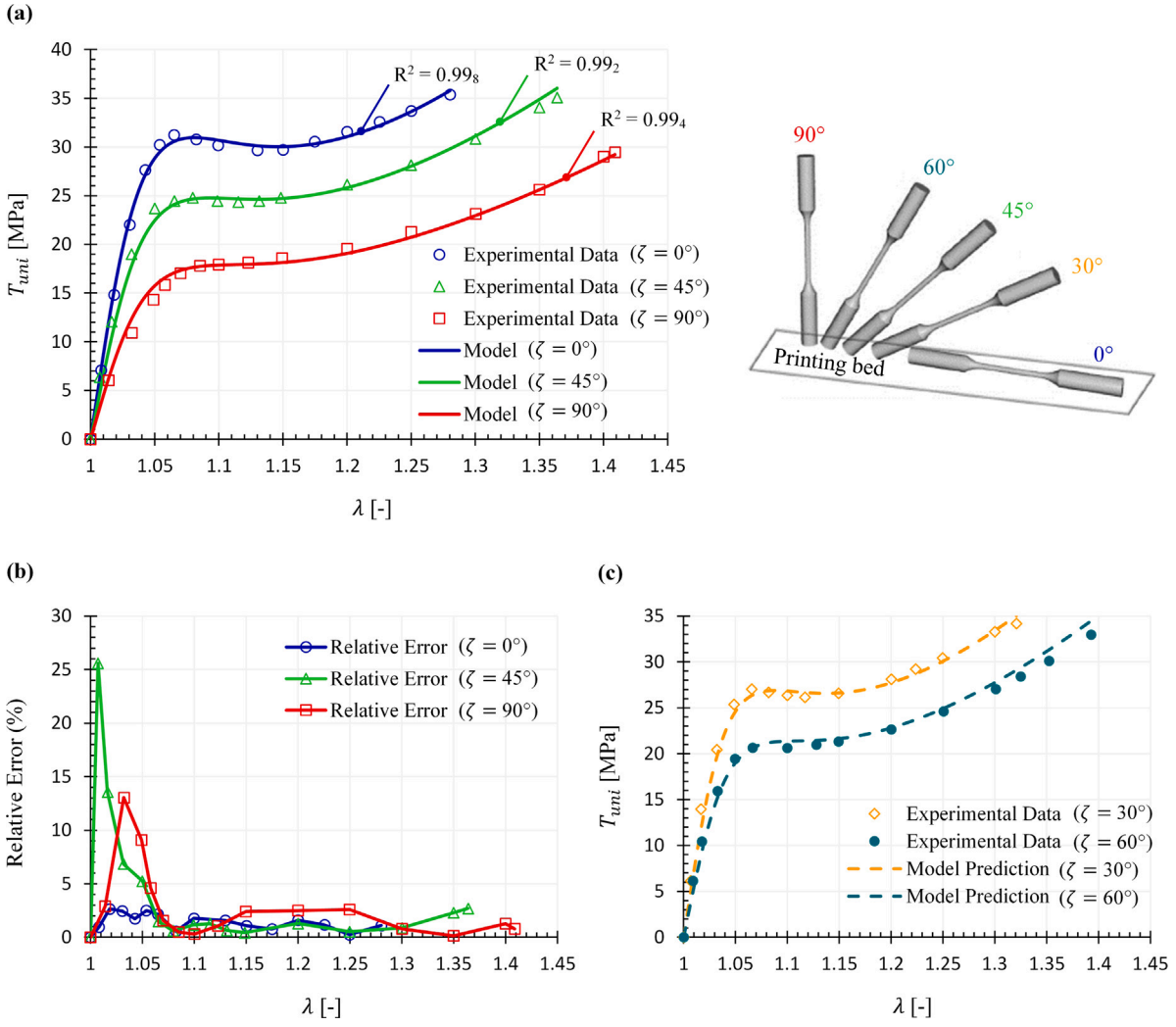

Fig. 12. Modelling the effect of the 3D printing angle (with respect to the printing bed) on the mechanical behaviour of additively manufactured specimens made from a curable photosensitive resin due to Guo et al. (2024): (a) fitting of the one-term expansion of the *augmented* model with the datasets of 0°, 45° and 90° specimens; (b) the ensuing relative errors; and (c) model *predictions* of the behaviour of the 30° and 60° specimens. The inset in panel (a) is a schematic representation to illustrate the orientation angle of the 3D printed specimens with respect to the printing bed. See the online version for plots in colour.
Source: Adapted from Guo et al. (2024) with permission.

the existing strain energy functions in the literature may be recovered, as discussed in Section 2.2. The model was then successfully applied to the large elastic and inelastic deformation behaviours of a variety of polymer and elastomer specimens, ranging from semi-crystalline and glossy polymers to foams, hydrogels and LCEs, as demonstrated in Section 3.

The *core* model was then *augmented* in Section 4 to incorporate other-than-deformation-induced inelastic effects, including the deformation rate, crystallinity volume ratio and even a factor such as the orientation angle of a 3D printed specimen with respect to the printing bed. For doing so, a generalised framework was devised and developed by taking into consideration a generic tensorial field as the additional inelasticity-inducing factor $\boldsymbol{\xi}$, which can then be specialised to represent various inelasticity-inducing factors of tensorial nature such as the rate of deformation tensor, to rank zero (i.e., scalar) factors such as crystallinity ratio ν_c etc. Upon defining an appropriate measure of those fields, denoted in this work by ζ, and considering suitable functional dependencies of the *core* model parameters on ζ, the *augmented* model $W^\star \equiv W(\mathbf{F}, \boldsymbol{\xi})$ is obtained. The successful application of the *augmented* model to various datasets and specimens in Section 4.3.1 to 4.3.3 demonstrated the favourability and versatility of this modelling framework, including its capability for *predicting* the behaviour of the specimens at different values of the designated ζ. While not considered here, the proposed *core hyperinelastic* model $W(\mathbf{F})$ may also be extended for capturing the inelastic behaviour in the unloading path.

Detailed frameworks of how this extension may be achieved have already been presented in Part I, as well as in Anssari-Benam et al. (2023) and Anssari-Benam and Hossain (2023; 2024).

Given the favourability of the *hyperinelasticity* approach presented in Part I and herein to capture the large elastic and inelastic behaviours of a wide range of different polymers, and the successful applications of the principal invariants- and stretches-based models therein and here to various samples and datasets, the devised modelling framework and models may be considered as convenient and accurate primary tools for capturing the complex inelastic behaviour of (various) polymers. Depending on the number of term expansions, the *core* models contain comparatively a low number of model parameters. As the examples herein and in Part I indicate, generally a two-term expansion of the models suffices, which only contains 10 and 12 model parameters, respectively. These will reduce to 5 and 6 if the one-term expansion of the models is used. Compared with other constitutive models in the literature, and the accuracy that they provide, these number of parameters are on the lower end of the spectrum.

Moreover, incorporation of additional inelasticity-inducing factors using the presented generalised framework in Section 4 into the model offers more flexibility in capturing such features, from rate-dependency to more obscure factors such as the angle of 3D printing. The combination of these attributes in a single modelling approach is rare in the literature, to the knowledge of the author, and provides more attraction for utilising the presented *hyperinelasticity* modelling framework.

CRediT authorship contribution statement

Afshin Anssari-Benam: Writing – review & editing, Writing – original draft, Validation, Software, Methodology, Formal analysis, Data curation, Conceptualization.

Declaration of competing interest

I have no competing interests to declare.

Data availability

The numerical values of the experimental datapoints used in this work have either been provided in Part I (Anssari-Benam, 2024b), Anssari-Benam (2024a) or presented in Appendix, Tables A.1 to A.4, of the manuscript.

Acknowledgements

Computational aspects of this work were carried out via the computing facilities generously remunerated from a concurrent Leverhulme Trust-funded project, via grant VP1-2023-002.

Appendix. Tabulated numerical datapoints of the datasets used in this work

Table A.1
Numerical datapoints from G'Sell et al. (2002) for the uniaxial tensile deformation of high-impact polystyrene specimens at ambient temperature.

λ [–]	T_{uni} [MPa]
1	0
1.00_{09}	2.38
1.00_{2}	5.71
1.00_{4}	11.77
1.00_{8}	18.58_{5}
1.01	24.05
1.02	22.20
1.03	20.05_{5}
1.05	18.40
1.09	18.20
1.13_{5}	18.68
1.19	19.29
1.23	19.90_{5}
1.28	20.55
1.31	20.83
1.36	21.21

Table A.2
Numerical datapoints for the quasi-static and rate-dependent deformation of amorphous polylactic acid (PLA) specimens under uniaxial compression due to Pan et al. (2024).

Quasi-static		$\zeta = 0.01$ s^{-1}		$\zeta = 0.1$ s^{-1}	
ε [–]	T_{uni} [MPa]	ε [–]	T_{uni} [MPa]	ε [–]	T_{uni} [MPa]
0	0	0	0	0	0
-0.00_5	−10.30	-0.00_7	−15.45	−0.01	−20.96
−0.01	−26.63	−0.02	−47.07	−0.02	−52.10
−0.02	−51.83	−0.04	−83.35	−0.03	−69.93
−0.03	−75.27	−0.05	−98.80	−0.04	−89.65
-0.04_5	−83.79	−0.07	−82.99	-0.05_5	−111.88
−0.06	-68.87_5	−0.11	−57.84	−0.07	-90.36_5
−0.07	−55.74	−0.15	−50.30	-0.09_5	−68.49
-0.10_5	−46.86	−0.20	−48.68	−0.14	−58.20
−0.15	−41.54	−0.25	−44.91	−0.20	−51.24
−0.20	−39.05	−0.30	−44.19	−0.26	−47.78
−0.26	−37.63	−0.40	−43.83	-0.30_5	−45.63
−0.31	−36.92	−0.50	−44.55	−0.40	−42.75
−0.40	−36.92	−0.55	−45.27	−0.48	−42.04
−0.49	−37.63	−0.60	−45.99	−0.60	−42.75
−0.60	−39.05	−0.66	−47.07	−0.70	−44.91
−0.70	−41.18	−0.71	−48.32	−0.75	−46.71
−0.80	−42.60	−0.80	−51.02	−0.80	−48.14

Table A.3
Tabulated numerical datapoints for the uniaxial tension of semi-crystalline polyethylene samples of Yan et al. (2021), originally reported in Abdul-Hameed et al. (2014), with various crystallinity volume ratios.

$\nu_c = 15.1\%$ (base-line)		$\nu_c = 30\%$		$\nu_c = 72.4\%$	
λ [–]	T_{uni} [MPa]	λ [–]	T_{uni} [MPa]	λ [–]	T_{uni} [MPa]
1	0	1	0	1	0
1.06	0.54	1.05	2.32	1.01_5	5.13
1.13	1.08	1.14_5	5.13	1.04	11.25_5
1.20	1.52	1.29	6.72	1.09	15.09
1.30	1.93	1.42	8.20	1.19	14.85
1.40	2.27	1.55	9.08	1.30	15.79
1.50	2.58	1.73_5	10.67	1.42	15.73
1.64	2.85	1.91	12.34	1.55	16.22
1.78	3.36	2.08	13.49	1.70	16.46
1.93	3.70	2.29_5	14.81	1.85	17.49_5
2.17	4.44	2.48_5	16.39	2.02	17.62
2.35	4.92	2.74	18.59	2.21	18.29
2.61	5.73_5	3.11	21.32	2.42	19.20
3.02	7.13	3.45	23.78_5	2.64	19.57
3.27	8.01	3.87	27.75	2.88	21.06
3.51	8.93	4.22	31.09	3.14	22.58
3.75	9.78	4.62	34.70	3.43	24.14
4.11	11.30	5.01	38.93	3.75	26.20
4.56	13.38	5.42	43.50	4.10	29.53
4.96	15.11	5.64	45.90	4.48	32.85
5.19	16.23	5.75_5	47.50	4.90	38.25
5.71	18.61	5.99	50.50	5.35	43.21_5
6.08	20.41	6.11	52.50	5.87	53.19

Table A.4
Numerical datapoints collated from Guo et al. (2024) on uniaxial tensile deformation of additively manufactured (3D printed) specimens made of a curable photosensitive resin, with various printing angles in relation to the printing bed.

$\theta = 0°$		$\theta = 30°$		$\theta = 45°$		$\theta = 60°$		$\theta = 90°$	
λ [–]	T [MPa]	λ [–]	T [MPa]	λ [–]	T [MPa]	λ [–]	T [MPa]	λ [–]	T [MPa]
1	0	1	0	1	0	1	0	1	0
1.00_8	7.08	1.00_7	6.15	1.00_7	6.37	1.00_9	6.15	1.01_5	6.04
1.02	14.83	1.02	13.96	1.02	12.07	1.02	10.44	1.03	10.93
1.03	22.02	1.03	20.44	1.03	18.99	1.03	15.93	1.05	14.32
1.04	27.64	1.05	25.38_5	1.05	23.69	1.05	19.45	1.06	15.85
1.05	30.22_5	1.06_5	27.03	1.06_5	24.47	1.07	20.66	1.07	17.05
1.06_5	31.24	1.08	26.70	1.08	24.80	1.10	20.62_5	1.08_5	17.81
1.08	30.79	1.10	26.37	1.10	24.47	1.13	20.99	1.10	17.92
1.10	30.17	1.12	26.15	1.11_5	24.36	1.15	21.32	1.12	18.14
1.13	29.66	1.15	26.59	1.13	24.47	1.20	22.64	1.15	18.58
1.15	29.72	1.20	28.13	1.15	24.80_5	1.25	24.61_5	1.20	19.56
1.17_5	30.56	1.22	29.23	1.20	26.14_5	1.30	27.03	1.25	21.27
1.20	31.57	1.25	30.44	1.25	28.16	1.32_5	28.41	1.30	23.13
1.22_5	32.58	1.30	33.30	1.30	30.84	1.35	30.11	1.35	25.64
1.25	33.71	1.32	34.18	1.35	34.08	1.39	32.97	1.40	29.02
1.28	35.39			1.36	35.08			1.41	29.46

References

Abdel-Wahab, A.A., Ataya, S., Silberschmidt, V.V., 2017. Temperature-dependent mechanical behaviour of PMMA: Experimental analysis and modelling. Polym. Test. 58, 86–95. http://dx.doi.org/10.1016/j.polymertesting.2016.12.016.

Abdul-Hameed, H., Messager, T., Zaïri, F., Naït-Abdelaziz, M., 2014. Large-strain viscoelastic–viscoplastic constitutive modeling of semi-crystalline polymers and model identification by deterministic/evolutionary approach. Comput. Mater. Sci. 90, 241–252. http://dx.doi.org/10.1016/j.commatsci.2014.03.043.

Ames, N.M., Srivastava, V., Chester, S.A., Anand, L., 2009. A thermo-mechanically coupled theory for large deformations of amorphous polymers. Part II: Applications. Int. J. Plast. 25, 1495–1539. http://dx.doi.org/10.1016/j.ijplas.2008.11.005.

Anssari-Benam, A., 2021. On a new class of non-Gaussian molecular-based constitutive models with limiting chain extensibility for incompressible rubber-like materials. Math. Mech. Solids 26, 1660–1674. http://dx.doi.org/10.1177/10812865211001094.

Anssari-Benam, A., 2023. Large isotropic elastic deformations: On a comprehensive model to correlate the theory and experiments for incompressible rubber-like materials. J. Elasticity 153, 219–244. http://dx.doi.org/10.1007/s10659-022-09982-5.

Anssari-Benam, A., 2024a. A generalised $W\left(I_1, I_2\right)$ strain energy function of binomial form with unified applicability across various isotropic incompressible soft solids. Acta Mech. 235, 99–132. http://dx.doi.org/10.1007/s00707-023-03677-1.

Anssari-Benam, A., 2024b. Hyperinelasticity: An energy-based constitutive modelling approach to isothermal large inelastic deformation of polymers. Part I. J. Mech. Phys. Solids 192, 105790. http://dx.doi.org/10.1016/j.jmps.2024.105790.

Anssari-Benam, A., Akbari, R., Dargazany, R., 2023. Extending the theory of pseudo-elasticity to capture the permanent set and the induced anisotropy in the Mullins effect. Int. J. Non-Linear Mech. 156, 104500. http://dx.doi.org/10.1016/j.ijnonlinmec.2023.104500.

Anssari-Benam, A., Bucchi, A., Saccomandi, G., 2021. On the central role of the invariant I_2 in nonlinear elasticity. Internat. J. Engrg. Sci. 163, 103486. http://dx.doi.org/10.1016/j.ijengsci.2021.103486.

Anssari-Benam, A., Hossain, M., 2023. A pseudo-hyperelastic model incorporating the rate effects for isotropic rubber-like materials. J. Mech. Phys. Solids 179, 105347. http://dx.doi.org/10.1016/j.jmps.2023.105347.

Anssari-Benam, A., Hossain, M., 2024. A unified pseudo-elastic model of *continuous* and *discontinuous* softening in the finite deformation of isotropic soft solids. Int. J. Solids Struct. 290, 112670. http://dx.doi.org/10.1016/j.ijsolstr.2024.112670.

Anssari-Benam, A., Saccomandi, G., 2024a. Continuous softening as a state of hyperelasticity: Examples of application to the softening behavior of the brain tissue. J. Biomech. Eng. 146, 091009. http://dx.doi.org/10.1115/1.4065271.

Anssari-Benam, A., Saccomandi, G., 2024b. A model for capturing the *rate-dependent* mechanical behaviour of liquid crystal elastomers. Mech. Mater. 198, 105108. http://dx.doi.org/10.1016/j.mechmat.2024.105108.

Arruda, E.M., Boyce, M.C., 1993. A three-dimensional constitutive model for the large stretch behavior of rubber elastic materials. J. Mech. Phys. Solids 41, 389–412. http://dx.doi.org/10.1016/0022-5096(93)90013-6.

Ayoub, G., Makki, M., Kadri, R., Dargazany, R., Nait Abdelaziz, M., 2024. Micromechanical modeling of the effects of crystal content on the visco-hyperelastic-viscoplastic behavior and fracture of semi-crystalline polymers. Mech. Mater. 189, 104897. http://dx.doi.org/10.1016/j.mechmat.2023.104897.

Ayoub, G., Zaïri, F., Fréderix, Gloaguen, J.M., Naït-Abdelaziz, M., Seguela, R., Lefebvre, J.M., 2011. Effects of crystal content on the mechanical behaviour of polyethylene under finite strains: Experiments and constitutive modelling. Int. J. Plast. 27, 492–511. http://dx.doi.org/10.1016/j.ijplas.2010.07.005.

Ayoub, G., Zaïri, F., Naït-Abdelaziz, M., Gloaguen, J., 2010. Modelling large deformation behaviour under loading–unloading of semicrystalline polymers: Application to a high density polyethylene. Int. J. Plast. 26, 329–347. http://dx.doi.org/10.1016/j.ijplas.2009.07.005.

Dinari, A., Zaïri, F., Chaabane, M., Ismail, J., Benameur, T., 2021. Thermo-oxidative stress relaxation in carbon-filled SBR. Plast. Rubber Compos. Macro. Eng. 50, 425–440. http://dx.doi.org/10.1080/14658011.2021.1913385.

Fried, E., 2002. An elementary molecular-statistical basis for the mooney and rivlin–saunders theories of rubber elasticity. J. Mech. Phys. Solids 50, 571–582. http://dx.doi.org/10.1016/S0022-5096(01)00086-2.

Gent, A.N., 1996. A new constitutive relation for rubber. Rubber Chem. Technol. 69, 59–61. http://dx.doi.org/10.5254/1.3538357.

G'Sell, C., Hiver, J.M., Dahoun, A., 2002. Experimental characterization of deformation damage in solid polymers under tension, and its interrelation with necking. Int. J. Solids Struct. 39, 3857–3872. http://dx.doi.org/10.1016/S0020-7683(02)00184-1.

Guo, X., Wang, E., Yang, H., Zhai, W., 2024. Mechanical characterization and constitutive modeling of additively-manufactured polymeric materials and lattice structures. J. Mech. Phys. Solids 189, 105711. http://dx.doi.org/10.1016/j.jmps.2024.105711.

Holzapfel, G.A., 2000. Nonlinear Solid Mechanics: A Continuum Approach for Engineering. John Wiley and Sons Ltd, Chichester, England, pp. 161–176.

Horgan, C.O., Saccomandi, G., 2003. Finite thermoelasticity with limiting chain extensibility. J. Mech. Phys. Solids 51, 1127–1146. http://dx.doi.org/10.1016/S0022-5096(02)00144-8.

Kearsley, E.A., 1989. Note: Strain invariants expressed as average stretches. J. Rheol. 33, 757–760. http://dx.doi.org/10.1122/1.550063.

Khiêm, V.N., Itskov, M., 2016. Analytical network-averaging of the tube model: Rubber elasticity. J. Mech. Phys. Solids 96, 254–269. http://dx.doi.org/10.1016/j.jmps.2016.05.030.

Kuhl, E., Goriely, A., 2024. I too ♥ I_2: A new class of hyperelastic isotropic incompressible models based solely on the second invariant. J. Mech. Phys. Solids 188, 105670. http://dx.doi.org/10.1016/j.jmps.2024.105670.

Lee, J.H., Ryu, D.M., Lee, C.S., 2020. Constitutive-damage modeling and computational implementation for simulation of elasto-viscoplastic-damage behavior of polymeric foams over a wide range of strain rates and temperatures. Int. J. Plast. 130, 102712. http://dx.doi.org/10.1016/j.ijplas.2020.102712.

Li, X., Roth, C.C., Tancogne-Dejean, T., Mohr, D., 2020. Rate- and temperature-dependent plasticity of additively manufactured stainless steel 316L: Characterization, modeling and application to crushing of shell-lattices. Int. J. Impact Eng. 145, 103671. http://dx.doi.org/10.1016/j.ijimpeng.2020.103671.

Makki, M., Ayoub, G., Pannier, C., Dargazany, R., Kadri, R., Nait Abdelaziz, M., Nouri, H., 2023. Micromechanical modeling of the visco-hyperelastic–viscoplastic behavior and fracture of aged semicrystalline polymers. Int. J. Non-Linear Mech. 155, 104456. http://dx.doi.org/10.1016/j.ijnonlinmec.2023.104456.

Ogden, R.W., 1972. Large deformation isotopic elasticity – on the correlation of theory and experiment for incompressible rubberlike solids. Proc. R. Soc. Lond. Ser. A Math. Phys. Eng. Sci. 326, 565–584. http://dx.doi.org/10.1098/rspa.1972.0026.

Ogden, R.W., 1997. Non-Linear Elastic Deformations. Dover Publications Inc, Mineola, New York, USA.

Ogden, R.W., Saccomandi, G., Sgura, I., 2004. Fitting hyperelastic models to experimental data. Comput. Mech. 34, 484–502. http://dx.doi.org/10.1007/s00466-004-0593-y.

Pan, Z., Chen, H., Brassart, L., 2024. Constitutive modelling of glassy polymers considering shear plasticity and craze yielding. Int. J. Plast. 178, 103996. http://dx.doi.org/10.1016/j.ijplas.2024.103996.

Puglisi, G., Saccomandi, G., 2016. Multi-scale modelling of rubber-like materials and soft tissues: *an appraisal*. Proc. R. Soc. A 472, 20160060. http://dx.doi.org/10.1098/rspa.2016.0060.

Richeton, J., Ahzi, S., Vecchio, K.S., Jiang, F.C., Adharapurapu, R.R., 2006. Influence of temperature and strain rate on the mechanical behavior of three amorphous polymers: Characterization and modeling of the compressive yield stress. Int. J. Solids Struct. 43, 2318–2335. http://dx.doi.org/10.1016/j.ijsolstr.2005.06.040.

Rivlin, R.S., 1948. Large elastic deformations of isotropic materials IV. Further developments of the general theory. Philos. Trans. R. Soc. Lond. Ser. A 241, 379–397. http://dx.doi.org/10.1098/rsta.1948.0024.

Sun, Z.P., Guo, Y.B., Shim, V.P.W., 2022. Influence of printing direction on the dynamic response of additively-manufactured polymeric materials and lattices. Int. J. Impact Eng. 167, 104263. http://dx.doi.org/10.1016/j.ijimpeng.2022.104263.

Tokumoto, H., Zhou, H., Takebe, A., Kamitani, K., Kojio, K., Takahara, A., Bhattacharya, K., Urayama, K., 2021. Probing the in-plane liquid-like behavior of liquid crystal elastomers. Sci. Adv. 7, eabe9495. http://dx.doi.org/10.1126/sciadv.abe9495.

Treloar, L.R.G., 1943. The elasticity of a network of long-chain molecules - II. Trans. Faraday Soc. 39, 241–246. http://dx.doi.org/10.1039/TF9433900241.

Treloar, L.R.G., 1976. The mechanics of rubber elasticity. Proc. R. Soc. Lond. Ser. A Math. Phys. Eng. Sci. 351, 301–330. http://dx.doi.org/10.1098/rspa.1976.0144.

Uchida, M., Kamimura, K., Yoshida, T., Kaneko, Y., 2022. Viscoelastic-viscoplastic modeling of epoxy based on transient network theory. Int. J. Plast. 153, 103262. http://dx.doi.org/10.1016/j.ijplas.2022.103262.

Vernerey, F.J., Brighenti, R., Long, R., Shen, T., 2018. Statistical damage mechanics of polymer networks. Macromolecules 51, 6609–6622. http://dx.doi.org/10.1021/acs.macromol.8b01052.

Yan, Z., Guo, Q., Zaïri, F., Zaoui, A., Jiang, Q., Liu, X., 2021. Continuum-based modeling large-strain plastic deformation of semi-crystalline polyethylene systems: Implication of texturing and amorphicity. Mech. Mater. 162, 104060. http://dx.doi.org/10.1016/j.mechmat.2021.104060.

Zhan, L., Wang, S., Qu, S., Steinmann, P., Xiao, R., 2023. A new micro–macro transition for hyperelastic materials. J. Mech. Phys. Solids 171, 105156. http://dx.doi.org/10.1016/j.jmps.2022.105156.